J. Fluid Mech. (2006), *vol.* 548, *pp.* 17–48. © 2006 Cambridge University Press
doi:10.1017/S002211200500738X Printed in the United Kingdom

Flow structure, momentum and heat transport in a two-tandem-cylinder wake

By Y. ZHOU AND M. W. YIU

Department of Mechanical Engineering, The Hong Kong Polytechnic University, Hung Hom, Kowloon, Hong Kong

(Received 1 November 2004 and in revised form 20 July 2005)

Flow structure, momentum and heat transport in the wake of two tandem circular cylinders have been experimentally investigated. Measurements were conducted at $x/d = 10$, 20 and 30 (d is the cylinder diameter) at a Reynolds number of 7000 using a three-wire (one cross-wire plus a cold wire) probe, in conjunction with a cross-wire. The upstream cylinder was slightly heated. The flow behind two tandem cylinders is conventionally divided into three regimes based on whether the shear layers separated from the upstream cylinder overshoot or reattach on the downstream cylinder before forming a vortex street, or form vortices between the cylinders. The present investigation uncovers two remarkably different flow structures in the reattachment regime, depending on whether the shear layers from the upstream cylinder reattach on the downstream or upstream side of the downstream cylinder. As such, four cylinder centre-to-centre spacing ratios, i.e. $L/d = 1.3$, 2.5, 4.0 and 6.0, were examined, each representing one distinct flow structure. The phase-averaged sectional streamlines and vorticity contours display a single vortex street, irrespective of different regimes. However, the detailed flow structure, in particular, the vortex strength, and its downstream development depend upon L/d. The cross-stream distributions of the Reynolds stresses and heat fluxes at a given x/d vary from one to another. Such variation is also evident in the coherent contributions to the Reynolds stresses and heat fluxes. The results are connected to different initial conditions for the four flow structures. The momentum and heat transport characteristics are summarized for each flow structure.

1. Introduction

Multiple structures immersed in a crossflow are frequently seen in engineering. One example is a cluster of high-rise skyscrapers, which characterize modern cities such as Hong Kong. These tall buildings have a significant influence on the flow and dispersion of gaseous pollutants that are discharged from a vast number of internal combustion vehicles and other fume pollutant sources. It is thus of practical importance to understand the flow and pollutant transport characteristics around multiple slender structures. Pollutant transport and dispersion is related to mass transfer and its investigation remains a challenge. Fortunately, the mechanisms of mass transfer mimic those of heat transfer (Lewis 1922) given that both mass and heat are passive scalars (Shraiman & Siggia 2000). The importance and relevance of the passive scalar to turbulent mixing, pollution and many other engineering settings has been elucidated in reviews by Warhaft (2000), Shraiman & Siggia (2000) and Antonia & Orlandi (2003). As such, it is a natural choice to use passive heat transport to simulate

pollutant transport, for heat transfer experiments are much easier to implement in laboratories.

The simplest configuration of multiple slender structures is two cylinders in tandem, side-by-side or staggered arrangements. Aerodynamic interference between two cylinders may give rise to flow separation, reattachment, vortex impingement, recirculation and quasi-periodic vortices, involving most of the generic flow features associated with multiple structures. Thus, flow around two cylinders provides a good model for gaining insight into flow physics and passive scalar transport around more structures.

Matsumura and Antonia (1993) investigated momentum and passive heat transport in the turbulent intermediate wake of a single circular cylinder at a Reynolds number Re ($\equiv U_\infty d/\nu$, where U_∞, d and ν are the free-stream velocity, cylinder diameter and kinematic viscosity of fluid, respectively) of 5830. There are few investigations, similar to Matsumura and Antonia (1993), behind two cylinders. Zhou, Zhang & Yiu (2002) studied momentum and heat transport in the wake of the two side-by-side cylinders, which had a transverse spacing $T/d = 1.5$ to 3.0 ($Re = 5800$). They found that the turbulent flow structures, heat and momentum transport depended on T/d and furthermore showed a remarkable difference from its counterpart in an isolated cylinder wake.

We may surmise that the manner in which momentum and heat are transferred behind two tandem cylinders must be different from that behind an isolated cylinder or two side-by-side cylinders. There have been numerous investigations on the flow behind two tandem circular cylinders, most of which focus on the Strouhal numbers, Re effects and forces on the cylinders (e.g. Zdravkovich 1977, 1987; Igarashi 1981; Arie *et al.* 1983; Ohya, Okajima & Hayashi 1989; Mahir & Rockwell 1996). This flow depends on the longitudinal spacing ratio L/d between the cylinder axes as well as Re, initial conditions and pressure gradient, etc. Zdravkovich (1987) classified the flow into three regimes based on L/d: (i) the extended-body regime, where L/d ranged from 1 to 1.2–1.8 and the two cylinders were so close to each other that the free shear layers separated from the upstream cylinder overshot the downstream one; (ii) the reattachment regime, where L/d was between 1.2–1.8 and 3.4–3.8, and the shear layers reattached on the downstream cylinder; (iii) the co-shedding regime, where L/d exceeded 3.8 and the shear layers rolled up alternately, forming a vortex street in the gap between, as well as behind, the cylinders. Igarashi (1981) suggested a similar classification. Xu & Zhou (2004) noted that the reattachment regime may be extended from $L/d \approx 2$ to 5, and that the relationship between the Strouhal number, St ($\equiv f_s d/U_\infty$, where f_s is the dominant vortex frequency), and Re at $L/d = 2$ to 3 was markedly different from that at $L/d = 3$ to 5. The different St–Re relationship was found to arise from different transition processes: with increasing Re a transition occurred from the extended-body regime to the reattachment regime for $L/d = 2$ to 3, but from the reattachment regime to the co-shedding regime for $L/d = 3$ to 5. Therefore, they proposed a new classification of the flow, i.e. four different flow categories, as illustrated in figure 1.

Previous investigations have greatly improved our understanding of this flow. However, many issues remain unresolved. For example, how is the detailed flow structure behind the cylinders dependent upon the flow regime? Is the flow structure at $L/d = 2$ to 3 different from that at $L/d = 3$ to 5? Furthermore, the associated temperature (or passive scalar) field has yet to be better understood. Therefore, one objective of this work is to study the effect of L/d on the flow structure in terms of the velocity and temperature fields. There has been a lack of information on the

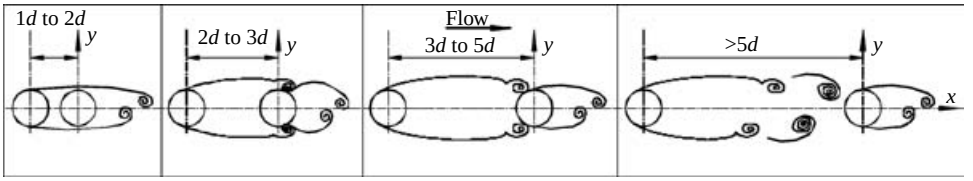

FIGURE 1. Sketches of four different flow structures.

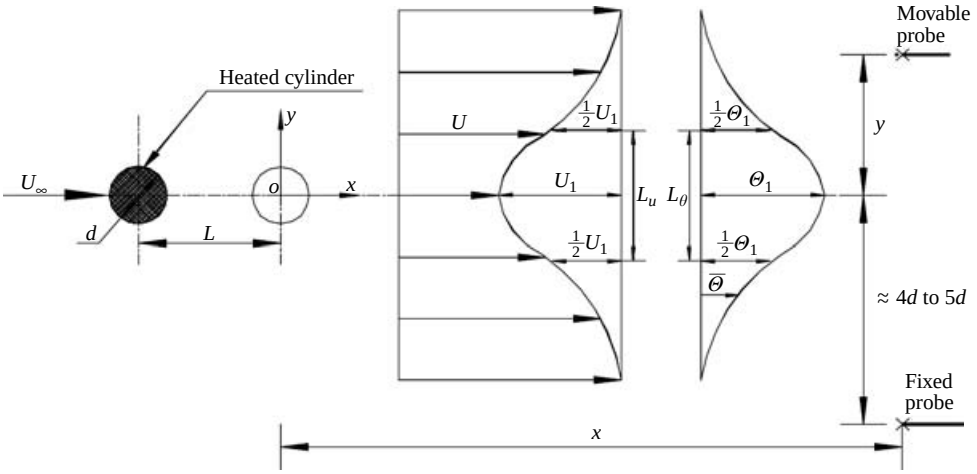

FIGURE 2. Experimental arrangement.

momentum and heat transport of this flow in the literature. The second objective is to investigate how the presence of a downstream cylinder affects the momentum and heat transport in a circular cylinder wake and how the transport differs between the flow regimes.

Experimental details are provided in § 2. Section 3 presents the time-averaged flow and temperature fields, followed by the phase-averaged results (§ 4). Section 5 documents the contribution from the coherent structures to the Reynolds stresses and heat fluxes. The momentum and heat transport characteristics are summarized in § 6 and the work is concluded in § 7.

2. Experimental arrangement

Experiments were conducted in a closed-circuit wind tunnel with a square cross-section (0.6 m × 0.6 m) of 2.4 m long. The wake was generated by two brass circular cylinders of the same diameter $d = 0.015$ m in the tandem arrangement (figure 2). Four different L/d ratios, i.e. 1.3, 2.5, 4.0 and 6.0, were investigated, representing the four flow categories (figure 1). The cylinders were placed horizontally in the mid-plane and spanned the full width of the working section, resulting in a maximum blockage of about 2.5 % and an aspect ratio of 40. The upstream cylinder was placed 0.2 m downstream of the exit plane of the contraction and was electrically slightly heated. The surface temperature of this cylinder was measured using both thermocouple and optic-fibre Bragg grating sensor (Wang *et al.* 2003) and was about 36 °C at $U_\infty = 7\,\mathrm{m\,s^{-1}}$. The ambient temperature was maintained at 24 °C. The maximum mean temperature of the heated wake at $x/d = 10$ (see figure 2 for the definition of

$\overline{U}^*$	$\overline{\Theta}^*$	u^*_{rms}	v^*_{rms}	$\overline{uv}^*$	θ^*_{rms}	St	y^*_c	U^*_c	$\tilde{\omega}^*$
± 2	± 3	± 5	± 6	± 6	± 5	± 1	± 3	± 3	± 6

TABLE 1. Percentage experimental uncertainties ($x/d = 10$ for y^*_c, U^*_c and $\tilde{\omega}^*$).

the coordinate system) did not exceed 1°C above ambient. The experimental data of a single cylinder wake obtained under similar experimental conditions by Zhou *et al.* (2002) were compared with those obtained by Zhou *et al.* (2003) without the cylinder being heated. The Reynolds normal stresses (not shown here) at $x/d = 10$ displayed a good collapse; the corresponding phase-averaged vorticity contours (not shown) also agreed reasonably well. The comparison provides convincing evidence for a negligible buoyancy effect, that is, heat could be considered as a passive scalar. Measurements were carried out at $U_\infty = 7\,\mathrm{m\,s^{-1}}$, corresponding to $Re = 7000$. In the free stream, the longitudinal turbulence intensity was measured to be no more than 0.4 %.

A three-wire probe consisting of a cross-wire probe and a cold wire were used to measure simultaneously the longitudinal velocity (u), transverse velocity (v) and temperature (θ) fluctuations. The cold wire was orthogonally orientated to the plane of the cross-wire and placed about 0.8 mm upstream of the cross-wire intersection. Thus, u, v and θ may be considered to be obtained at nominally the same point. Another cross-wire, placed at $y = -(4d$ to $5d)$, depending on the measurement station x/d (=10 to 30), was used in conjunction with the three-wire probe in order to provide a phase reference for the measured velocity signals from the three-wire probe. The sensing elements of the cross-wires were made of 5 μm Wollaston wire (Pt-10 % Rh) of approximately 1 mm in length, operated on constant temperature circuits at an overheat ratio of 1.5. The sensing element of the cold wire was made of 1.27 μm Wollaston wire (Pt-10 % Rh), which was about 1.2 mm in length. The cold wire was operated in a constant current (0.1 mA) circuit with an output proportional to θ. The temperature coefficient of the cold wire was estimated to be $1.69 \times 10^{-3}\ \mathrm{K^{-1}}$. Velocity and temperature signals from the anemometers were passed through buck and gain circuits, low-pass filtered and digitized on a personal computer using a 12 bit A/D converter at a sampling frequency $f_{sampling} = 3500$ Hz per channel. The sampling duration was 30 s.

Experimental uncertainties in $\overline{U}$, $\overline{\Theta}$, u_{rms} or v_{rms}, and θ_{rms} are given in table 1, where U is the instantaneous streamwise velocity, $\overline{\Theta}$ is the instantaneous temperature, overbar and subscript *rms* represent the time-averaged quantity and root mean square value, respectively. The uncertainties in $\overline{U}$, u_{rms} or v_{rms}, were inferred from errors in the hot-wire calibration data, and those in $\overline{\Theta}$ and θ_{rms} were largely due to errors in the cold-wire's drifting during measurements and a slow change in surrounding conditions.

3. Time-averaged flow and temperature fields

The cross-stream distributions of $\overline{U}^*$ and $\overline{\Theta}^*$ are shown in figure 3. The asterisk indicates hereinafter normalization by U_∞, d and the maximum mean temperature excess, Θ_1, in the wake. The $\overline{U}^*$ profiles display one single peak and reasonable symmetry about $y^* = 0$, irrespective of the L^* value, suggesting the occurrence of a single vortex street. However, there is a considerable variation in their peak values,

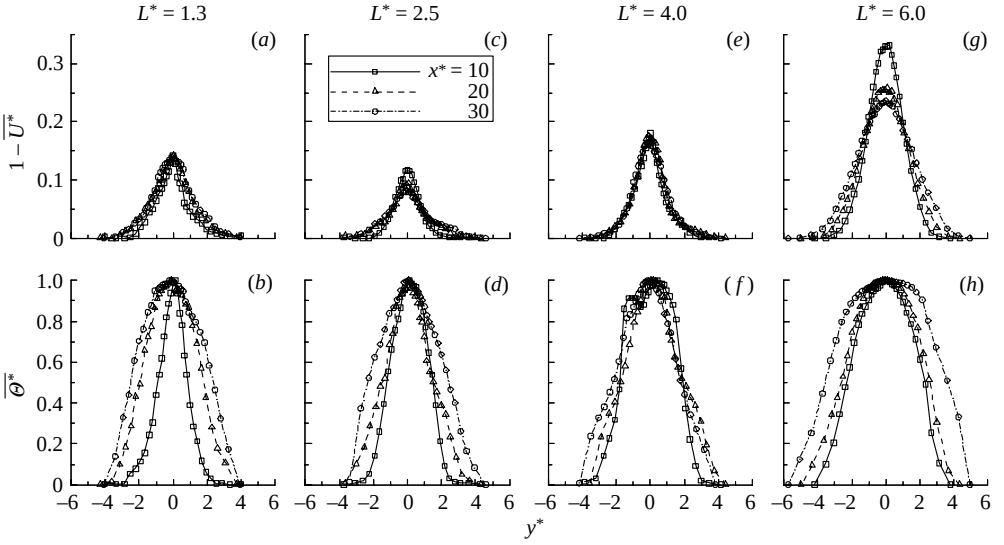

FIGURE 3. Time-averaged streamwise velocity $\overline{U}^*$ and temperature $\overline{\Theta}^*$.

L^*	1.3			2.5			4.0			6.0		
x^*	10	20	30	10	20	30	10	20	30	10	20	30
U_1^*	0.143	0.142	0.139	0.116	0.095	0.080	0.180	0.176	0.165	0.331	0.258	0.235
Θ_1	1.06	0.46	0.44	0.87	0.45	0.42	0.69	0.69	0.47	0.6	0.46	0.19
L_u^*	1.50	2.20	2.41	1.64	1.76	2.34	1.67	1.83	2.11	2.39	3.18	3.88
L_θ^*	1.72	4.04	4.84	2.75	3.02	4.78	3.67	3.75	3.99	4.58	5.23	7.16

TABLE 2. Maximum velocity defect, temperature excess and half-widths.

that is, their maximum mean velocity deficits, U_1, differ from one case to another. Similarly to $\overline{U}^*$, values of $\overline{\Theta}^*$ exhibit one single peak.

Table 2 summarizes the major characteristic properties of the mean flow and temperature fields. As x^* increases from 10 to 30, U_1 and Θ_1 diminish, which is expected, and the mean velocity half-width L_u grows by 60 %, 43 %, 26 % and 62 % for $L^* = 1.3$, 2.5, 4.0 and 6.0, respectively. Evidently, the wake growth is slow at $L^* = 2.5$ and 4.0 of the reattachment regime, but is faster in other regimes, i.e. at $L^* = 1.3$ and 6.0. Correspondingly, the mean temperature half-width L_θ grows by 180 %, 74 %, 9 % and 56 % for $L^* = 1.3$, 2.5, 4.0 and 6.0, respectively. The growth in L_u and L_θ will be linked in §§ 4 and 5 to the distinct behaviours of coherent structures and subsequently heat and momentum transport among the four flow structures.

4. Phase-averaged flow and temperature fields

4.1. *Phase-averaging technique*

The flow behind two tandem cylinders is characterized by quasi-periodic large-scale structures, irrespective of flow regimes, as evidenced in the power spectral density functions, E_u, E_v and E_θ (figure 4), of u, v and θ measured at $x^* = 10$ and $y^* = 1$, which display a pronounced peak at $St = 0.194$, 0.186, 0.144 and 0.190 for $L^* = 1.3$,

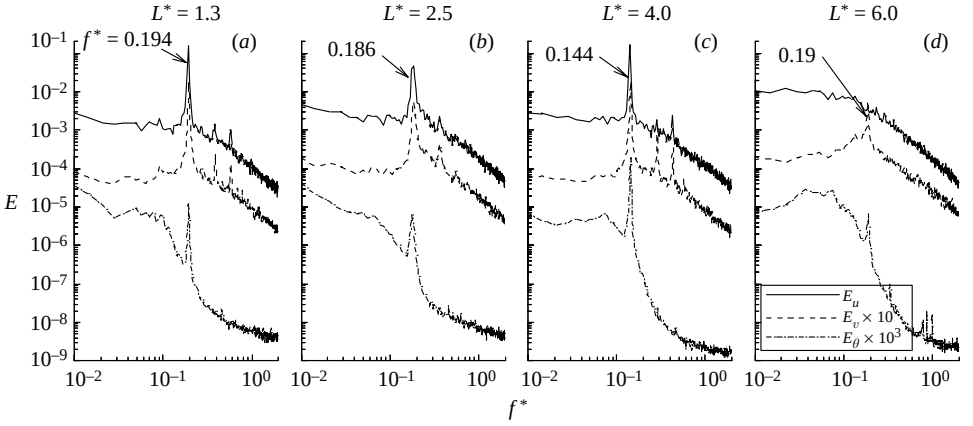

FIGURE 4. Power spectra of u, v and θ at $y^* = 1$ for $x^* = 10$.

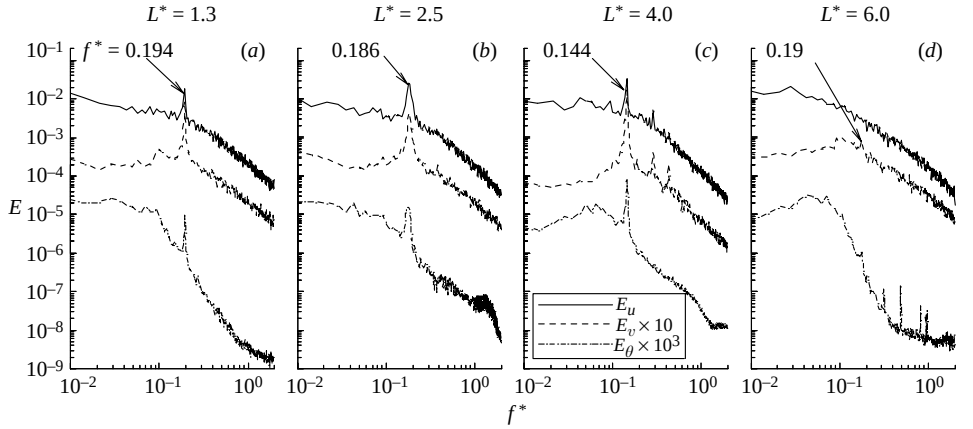

FIGURE 5. Power spectra of u, v and θ at $y^* = 1$ for $x^* = 30$.

2.5, 4.0 and 6.0, respectively. The second harmonic is also discernible in E_u and E_v for $L^* = 1.3$, 2.5 and 4.0. Note that at $L^* = 6.0$ the peak at $St = 0.190$ is considerably less pronounced in E_v or E_θ and almost invisible in E_u, suggesting relatively weak vortical structures. The St value at $L^* = 1.3$ is approximately the same as at $L^* = 6.0$. This should be coincidental. Xu & Zhou (2004) conducted a rather exhaustive measurement of St in the wake of two tandem cylinders over $Re = 800$ to 42000 and $L^* = 1$ to 15 using hot wires and reported that St varies with L^* as well as Re. The St values in figure 4 show reasonable agreement with Xu & Zhou's measurement for the same L^* and Re. As x^* increases to 30, the pronounced peak remains evident in the spectra for $L^* = 1.3$, 2.5 and 4.0 (figure 5*a–c*) but faintly discernible in E_v for $L^* = 6.0$ (figure 5*d*), suggesting a rapid annihilation of vortical structures in the co-shedding regime.

Figure 6 shows the v-signal from the three-wire probe for $L^* = 1.3$, 2.5, 4.0 and 6.0, respectively, along with the simultaneously obtained reference v_R-signals measured from the fixed cross-wire probe at $y^* = 4$. There is a clear phase relationship between the large events of v and v_R. Therefore, the experimental data are phase-averaged, based on the identification of the quasi-periodic large-scale events. The phase-averaging method is similar to that used by Antonia *et al.* (1993) and Zhou *et al.* (2002). Briefly, the v-signals from the movable three-wire probe and the fixed

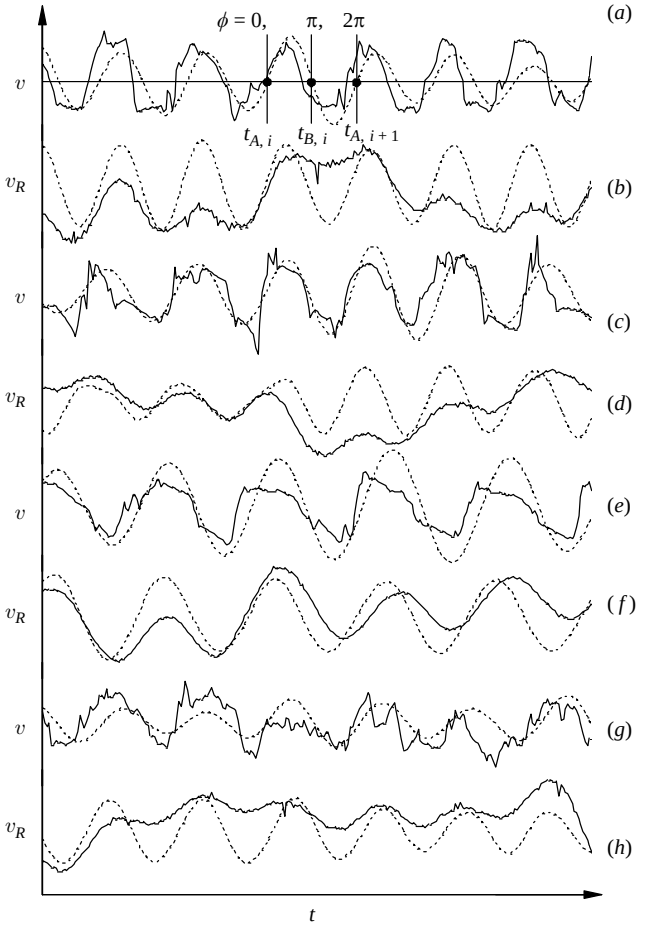

FIGURE 6. Signal v from the movable probe and v_R from the fixed probe. The dashed line represents the filtered signal v_f ($x^* = 10$, $y^* = 1$): (a, b) $L^* = 1.3$; (c, d) $L^* = 2.5$; (e, f) $L^* = 4.0$; (g, h) $L^* = 6.0$.

reference probe were both digitally band-pass filtered with the centre frequency set at f_s using a fourth-order Butterworth filter. The low- and high-pass frequencies were chosen to be the same as f_s, that is, a zero band-pass width was chosen in order to focus on the large-scale vortical structures. It was tested to allow the low- and high-pass frequencies to be slightly higher and lower, respectively, than f_s. The flow structure thus obtained was essentially unchanged. The phase shift caused by a fourth-order Butterworth filtering is very small, about 0.5 % of the vortex-shedding period, and almost identical for all signals since the shift depends largely on the filtering frequency set at f_s (Zhou *et al.* 2002).

The filtered signal v_f is given by the dashed line in figure 6. Two phases of particular interest are identified on v_f, namely,

$$\text{phase A:} \quad \frac{\mathrm{d}v_f}{\mathrm{d}t} > 0, \quad v_f = 0,$$

$$\text{phase B:} \quad \frac{\mathrm{d}v_f}{\mathrm{d}t} < 0, \quad v_f = 0.$$

The two phases correspond to time $t_{A,i}$ and $t_{B,i}$, respectively, which are measured from an arbitrary time origin. The filtered signal was used to determine the phase of the u-, v- and θ-signals from the three-wire probe, namely,

$$\phi = \pi \frac{t - t_{A,i}}{t_{B,i} - t_{A,i}}, \quad t_{A,i} \leqslant t \leqslant t_{B,i},$$

$$\phi = \pi \frac{t - t_{B,i}}{t_{A,i+1} - t_{B,i}} + \pi, \quad t_{B,i} \leqslant t \leqslant t_{A,i+1}.$$

The interval between phases A and B was made equal to $0.5T_s = 0.5/f_s$ by compressing or stretching and was further divided into 30 equal intervals. The measured (i.e. the original unfiltered) u-, v- and θ-signals from the three-wire probe were then phase-averaged at each y-location. The difference between the local phase of v at each y-location of the three-wire probe and the reference phase of v_R at the fixed cross-wire probe was used to determine the phase shift between the signals, which is essential to produce the phase-averaged or coherent data in the (ϕ, y)-plane.

The phase average of an instantaneous quantity Q is calculated by

$$\langle Q \rangle_k = \frac{1}{N} \sum_{i=1}^{N} Q_{k,i},$$

where k represents phase. For convenience, the subscript k will be omitted hereinafter. N is the total number of detections, about 2700, 2600, 2000 and 2500 for $L^* = 1.3$, 2.5, 4.0 and 6.0, respectively. Q can be viewed as the sum of the time mean component $\overline{Q}$ and the fluctuating component q. The latter is further decomposed into the coherent fluctuation $\tilde{q} \equiv \langle q \rangle$ and a remainder (incoherent fluctuation) q_r, namely,

$$q = \tilde{q} + q_r.$$

Also,

$$\langle qs \rangle = \tilde{q}\tilde{s} + \langle q_r s_r \rangle,$$

where q and s stand for either u, v or θ.

4.2. *Phase-averaged vorticity and sectional streamlines*

The phase-averaged vorticity is calculated by

$$\tilde{\omega} = \frac{\partial(\overline{V} + \tilde{v})}{\partial x} - \frac{\partial(\overline{U} + \tilde{u})}{\partial y} \approx \frac{\Delta \tilde{v}}{\Delta x} - \frac{\Delta(\overline{U} + \tilde{u})}{\Delta y},$$

where $\overline{V}$ (≈ 0) is the time-averaged velocity in the lateral direction, $\Delta x = -U_c \Delta t = -U_c / f_{sampling}$ and U_c is the average convection velocity at the vortex centre, which is identified with the location of the maximum phase-averaged vorticity $\tilde{\omega}_{max}$. Figures 7 and 8 present the iso-contours of the phase-averaged vorticity, $\tilde{\omega}^*$, and the corresponding sectional streamlines. The streamlines are viewed at a reference frame moving at U_c. The phase ϕ, ranging from -2π to $+2\pi$, can be explicated in terms of a longitudinal distance, $\phi = 2\pi$ corresponding to the average vortex wavelength. To avoid any distortion of the physical space, the same scales are used in the ϕ- and y^*-directions in figures 7 and 8 and others that follow. The positions of foci and saddle points (e.g. Zhou & Antonia 1994) associated with vortices are determined from sectional streamlines (figure 8) and denoted by '+' and '×', respectively. In general, the foci correspond well to the maximum vorticity, in particular, at $x^* = 10$. The $\tilde{\omega}^*$ contours (figure 7) and sectional streamlines (figure 8) display a single vortex

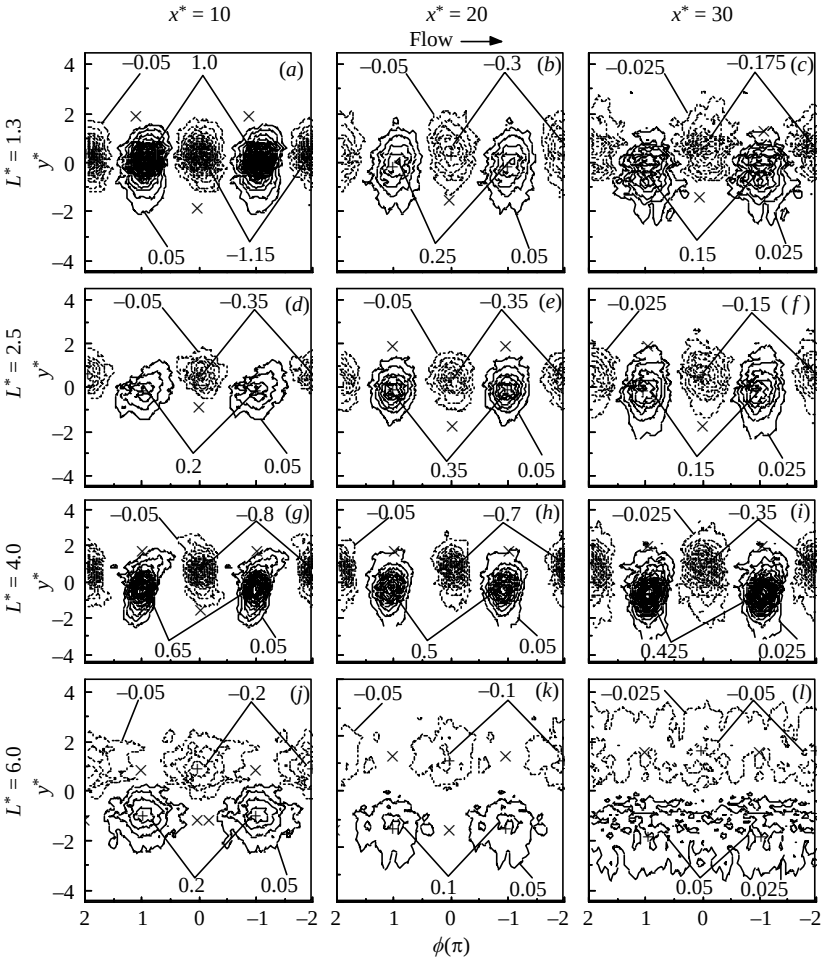

FIGURE 7. Phase-averaged vorticity contours $\tilde{\omega}^*$. (*a–c*) Contour interval = 0.05; 0.05; 0.025. (*d–f*) 0.05; 0.05; 0.025. (*g–i*) 0.05; 0.05; 0.025. (*j–l*) 0.05; 0.05; 0.025.

L^*	1.3			2.5			4.0			6.0		
x^*	10	20	30	10	20	30	10	20	30	10	20	30
y_c^*	0.18	0.36	0.62	0.5	0.41	0.58	0.63	0.82	0.93	0.92	1.18	1.67
U_c^*	0.87	0.91	0.92	0.92	0.93	0.96	0.91	0.92	0.93	0.79	0.85	0.86
$\tilde{\omega}_{max}^*$	−1.18	−0.30	−0.19	−0.37	−0.37	−0.16	−0.83	−0.75	−0.36	−0.24	−0.12	−0.07

TABLE 3. The vortex path, convection velocity and maximum vorticity.

street, regardless of the flow regimes, similar to that behind an isolated cylinder, i.e. $L^* = 0$, as suggested earlier by the cross-stream distributions of $\overline{U}^*$ and $\overline{\Theta}^*$.

Table 3 summarizes the most likely vortex location, y_c^*, U_c^* and $\tilde{\omega}_{max}^*$. Since the phase-averaged flow structure is reasonably anti-symmetrical about $y^* = 0$, only those associated with the upper-row vortices are given. The experimental errors in y_c^*, U_c^* and $\tilde{\omega}_{max}^*$ at $x^* = 10$ are given in table 1. The errors are expected to be greater for

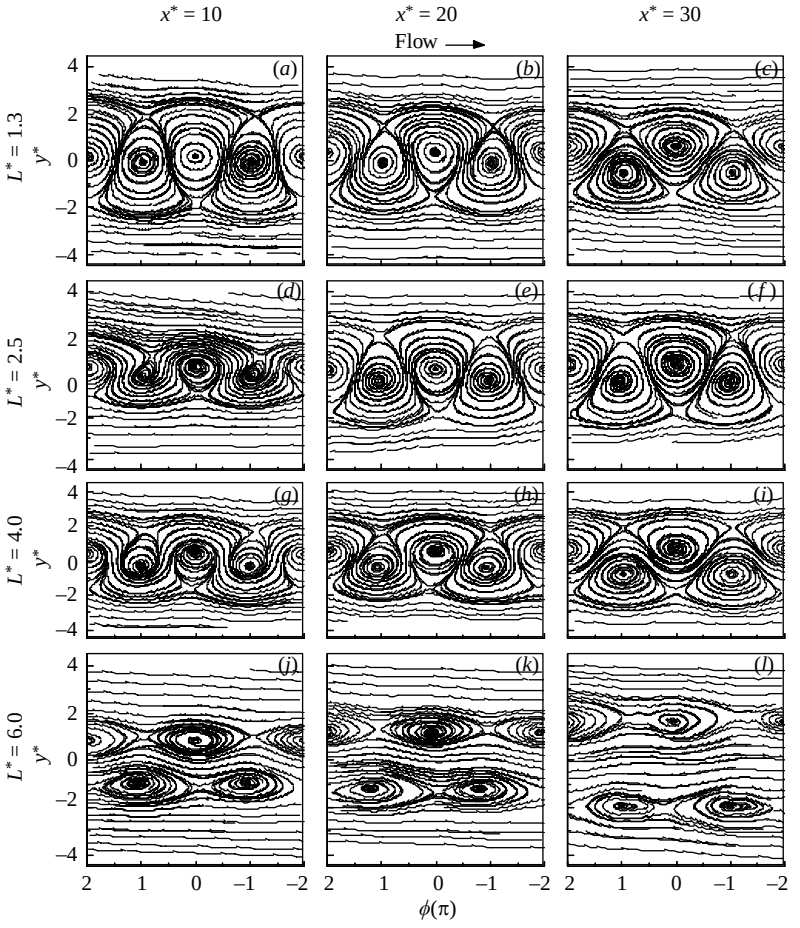

FIGURE 8. Phase-averaged sectional streamlines. The U_c^* values in table 2 are used in construction of sectional streamlines.

larger x^* owing to an increased unceratinty in determining the vortex centre. The y_c^* value increases from $x^* = 10$ to 30 by 240 %, 16 %, 48 % and 82 % for $L^* = 1.3$, 2.5, 4.0 and 6.0, respectively. The U_c^*values in the reattachment regime, i.e. at $L^* = 2.5$ and 4.0, are rather close to each other and are larger than that at $L^* = 1.3$. U_c^* at $L^* = 6.0$ is the smallest, which is consistent with the most pronounced velocity deficit (figure 3*g*). For all L^*, U_c increases with x^*, as observed behind an isolated cylinder wake (Zhou & Antonia 1994).

The magnitude $|\tilde{\omega}_{max}^*|$ of $\tilde{\omega}_{max}^*$ at $L^* = 1.3$ is largest of all regimes at $x^* = 10$, which is internally consistent with the most pronounced peak in the power spectra (figure 4). This magnitude is about 1.18 at $x^* = 10$ and 0.30 at $x^* = 20$, a drop of 75 %. Its counterpart at $L^* = 0$ is 1.19 at $x^* = 10$ and 0.52 at $x^* = 20$ (measured in the same facility by Zhou *et al.* 2002), decreasing by 56 %. The comparison suggests that the vortices behind two tandem cylinders decay more rapidly than that behind an isolated cylinder, though their initial strengths are comparable. At $x^* = 10$, the $|\tilde{\omega}_{max}^*|$ value is 0.83 at $L^* = 4.0$, exceeding twice that (0.37) at $L^* = 2.5$. Nonetheless, their decay rates are similar, $|\tilde{\omega}_{max}^*|$ dropping by 0 % and 12 % from $x^* = 10$ to 20 for $L^* = 2.5$ and 4.0, respectively. Note that the drop in $|\tilde{\omega}_{max}^*|$ from $x^* = 10$ to 30 is the

same, by 57 %, for the two cases. This may be ascribed to the fact that the shear layer reattachment on the downstream cylinder occurs in both cases. The decay rate of $|\tilde{\omega}^*_{max}|$ in the reattachment regime is significantly smaller than at $L^* = 1.3$, with $|\tilde{\omega}^*_{max}|$ sliding by 84 % from the value at $x^* = 10$ to 30. The $|\tilde{\omega}^*_{max}|$ value at $L^* = 6.0$ is smallest of all and decay rapidly. In fact, the vortex street is barely discernible at $x^* = 30$ (figures 7 and 8). For $L^* = 2.5$, $|\tilde{\omega}^*_{max}|$ at $x^* = 20$ is 0.37, the same as at $x^* = 10$. $|\tilde{\omega}^*_{max}|$ associated with the lower row increases from 0.25 at $x^* = 10$ to 0.35 at $x^* = 20$ (figure 7*d*–*e*). At $L^* = 4.0$, $|\tilde{\omega}^*_{max}|$ experiences a merely marginal decline from $x^* = 10$ to 20. Furthermore, the $\tilde{\omega}^*$ contours and sectional streamlines both display a discernible growth in the vortex size from $x^* = 10$ to 20 (figures 7*d*, *e* and 8*d*, *e*), suggesting that the vortex formation at $L^* = 2.5$ may not be completed until $x^* = 20$ or so. More discussion on the streamwise variation of vortices at $L^* = 2.5$ and 4.0 will be given later. Apparently, the vortices for these cases behave quite differently in terms of their lateral location, convection velocity, strength and decay rate, reflecting a difference between the flow structures in the four flow categories, even though they all display a single alternately arranged vortex street.

It can be pertinent to comment on some analogy between a two-tandem cylinder wake and that of a single cylinder with a splitter plate attached downstream. For $L^* < 2$, the downstream cylinder does not obstruct the vortex formation from the upstream cylinder. Similarly, a splitter plate of length $l \approx d$ does not inhibit the vortex formation, but causes 20 % or so reduction in *St* and 35 % increase in the base pressure when compared with the case of a plain cylinder (Roshko 1953, 1954, 1961). However, a splitter plate longer than $2d$ progressively modifies the base pressure and vortex shedding until l reaches $5d$, at or beyond which the flow separated from the cylinder reattaches on the splitter plate and vortex shedding is eliminated, although a quasi-periodical vortex street is formed far away from the cylinder (Apelt & West 1973, 1975). Grove *et al.* (1964) found that, at $Re = 25 \sim 300$, the splitter-plate effect in terms of stabilizing a steady wake was maximum when l was about $2d$ to $3d$. In the reattachment regime of a two tandem cylinder wake, vortex shedding, albeit not inhibited, is impaired, particularly at small L^* (≈2–3). In the co-shedding regime ($L^* \gtrsim 5$), vortex shedding from the upstream cylinder resumes. Likewise, Hasan & Budair (1994) observed in a square cylinder wake that, irrespective of the l/d value (d is the cylinder height), *St* varied with the gap, g/d, between the trailing edge of the cylinder and the leading edge of the splitter plate and, at $g/d \approx 6.0$, approached the value in the absence of the splitter plate.

4.3. *Phase-averaged temperature field*

Figure 9 presents the contours of the phase-averaged temperature, $\overline{\Theta^*} + \tilde{\theta}^*$. The outermost $\tilde{\omega}^*$ contour in figure 7 is included in the figure (and also those that follow) to mark approximately the vortex border. The higher isotherms of $\overline{\Theta^*} + \tilde{\theta}^*$, except at $L* = 6.0$, in general, exhibit a close similarity to the $\tilde{\omega}^*$ contours (figure 7), indicating the association of heat with vortices. However, this similarity fades at $x^* = 20$ for $L^* = 1.3$, suggesting a quick transport of heat out of vortical structures. The $\overline{\Theta^*} + \tilde{\theta}^*$ contours at$L^* = 2.5$ maintain strong concentrations at $x^* = 20$ (figure 9*d*, *e*) and do not lose the similarity to the $\tilde{\omega}^*$ contours until $x^* = 30$. The result is in line with the earlier observation that, unlike the other cases, the vortex at $L^* = 2.5$ (figures 7*d*, *e* and 8*d*, *e*) maintains its growth from $x^* = 10$ to 20 and starts to decay from $x^* = 20$ to 30. Since the vortex at $L^* = 4.0$ decays as slowly as at $L^* = 2.5$ (figures 7*g*, *i* and 8*g*, *i*) and further retains a significant strength at $x^* = 30$ (figure 8*i*), $\overline{\Theta^*} + \tilde{\theta}^*$ shows a high concentration even at $x^* = 30$ and coincides well with the $\tilde{\omega}^*$ concentration. The

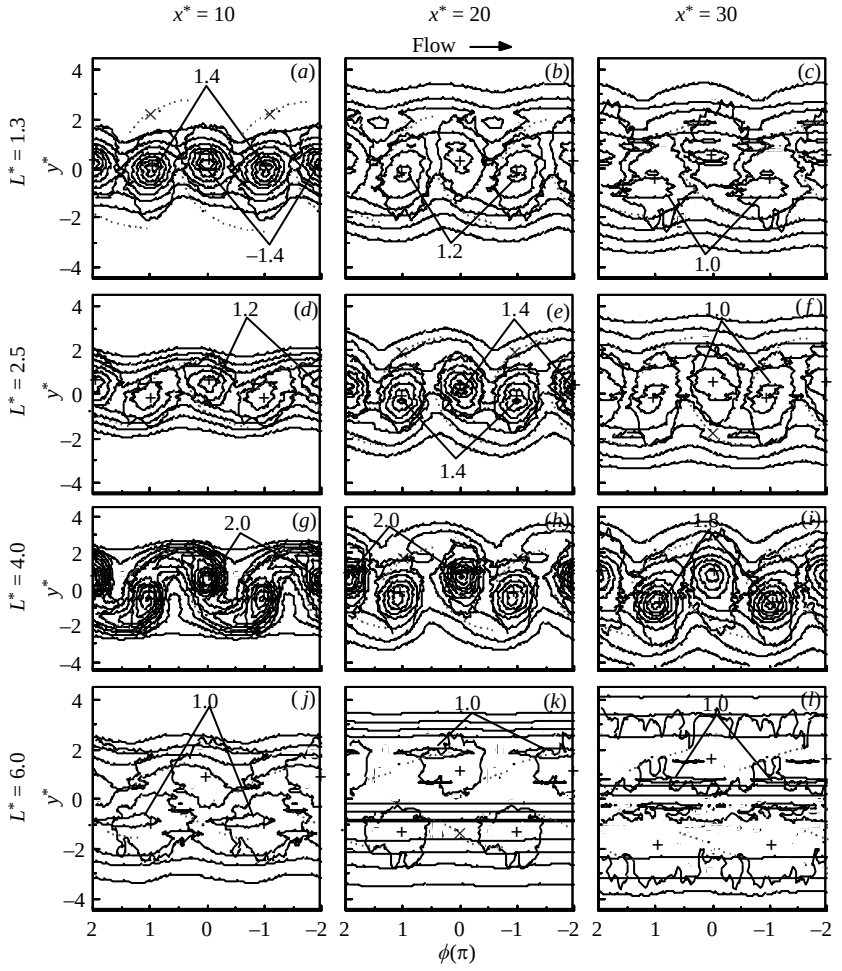

FIGURE 9. Phase-averaged temperature contours $\overline{\Theta}^* + \tilde{\theta}^*$. (*a–c*) Contour interval = 0.2; 0.2; 0.2. (*d–f*) 0.2; 0.2; 0.2. (*g–i*) 0.2; 0.2; 0.2. (*j–l*) 0.2; 0.2; 0.2. The thicker solid line denotes the outermost vorticity contours in figure 7; the broken line indicates the diverging separatrix.

lower isotherms except at $L^* = 6.0$ are drawn in towards the centreline downstream of each vortex, reflecting the arrival of cold fluid (from the free stream) in the alleyway between two opposite-signed vortices. The diverging separatrix through the saddle point is given as a broken line in figure 9. The separatrix intersects the isotherms at $L^* = 1.3$, similarly to the near wake of an isolated cylinder (Matsumura & Antonia 1993), but corresponds approximately to the temperature front, normal to which the temperature gradient is quite large, for other L^* values as observed for a cylinder far-wake (Antonia *et al.* 1987; Ferré and Giralt 1989).

The different behaviours of $\tilde{\omega}^*$ and $\overline{\Theta}^* + \tilde{\theta}^*$ between the three flow regimes may be traced back to the nature of flow interference between two tandem cylinders. At $L^* = 1.3$, shear layers separating from the upstream cylinder roll over behind the downstream cylinder to form a vortex street and the vortices show a fast decay (figure 7*a–c*). As L^* exceeds 5, vortices generated by the upstream cylinder impinge upon the downstream cylinder. Apparently, the incoming flow of the downstream cylinder is turbulent, which may postpone flow separation from the cylinder, resulting

in weak vortices (figures 7*j*, *l* and 8*j*, *l*). Since the coherent structures tend to retain heat (e.g. Matsumura & Antonia 1993; Zhou *et al.* 2002), the weak vortex will surely lead to a quick loss of heat associated with vortices, as evident in figure 9(*a–c*, *j–l*). At $L^* = 2.5$ and 4.0, the free shear layers from the upstream cylinder reattach on the downstream cylinder. The vortices of the two cases do differ significantly in strength. As a consequence, the heat concentration at $x^* = 30$ is strong and closely associated with the vortex for $L^* = 4.0$; but the same cannot be said for $L^* = 2.5$. The reattachment seems to have considerably prolonged the vortex formation process, and the vortical structures maintain their strength further downstream than the other two regimes. Correspondingly, the vortex-associated heat is diffused slowly.

It is worth commenting on the downstream evolution of vortices at $L^* = 2.5$. Since the vortex grows in both maximum vorticity and spatial extent (figure 8) from $x/d = 10$ to 20, the growth cannot be attributed to diffusion. Presumably, the observed vortices are largely, at least initially, attributed to the shedding of vorticity from the downstream cylinder, which is supported by Xu & Zhou's (2004) flow visualization (their figure 4). Vigorous interactions between vorticity separated from the upstream cylinder and that shed from the downstream cylinder could lead to a significant portion of vorticity scattered in the wake rather than mostly confined within the vortices, as with an isolated cylinder case and that at $L^* = 1.3$. Naturally, as the vortices are advected downstream, the roll-up of vorticity continues and the vortices keep growing until $x^* \approx 20$. The same may explain the slow decay of vortices at $L^* = 4.0$. The explanation appears to be supported by the observation that, at $L^* = 4.0$, both $\tilde{\omega}^*$ and $\overline{\Theta^*} + \tilde{\theta}^*$ contours towards the free-stream display a tail pointing upstream (figures 7*g* and 9*g*) at $x^* = 10$, conforming to the roll-up motion of vorticity. In contrast with the case at $L^* = 2.5$ or 4.0 where vorticity separated from the upstream cylinder reattaches on the downstream cylinder, at $L^* = 6$, vortices are formed between the gap of the two cylinders and impinge upon the downstream cylinder. Subsequently, vortices observed behind the downstream cylinder do not appear strongly coherent, when compared with the case at $L^* = 2.5$ (see figure 6 in Xu & Zhou 2004), and accordingly the roll-up of vorticity is simply too weak to be persistent.

4.4. *Vorticity transport*

It has been seen in § 4.2 that, as x^* increases from 10 to 30, the vortices at $L^* = 1.3$ and 6.0 lose their strength more rapidly than those in the reattachment regime, i.e. at $L^* = 2.5$ and 4.0. In order to understand the interaction between two vortex streets and the streamwise decay in vorticity in the turbulent wake of two side-by-side cylinders, Kolář, Lyn & Rodi (1997) and Zhou *et al.* (2002) employed the effective turbulent vorticity flux density vector, $\tilde{J} = \{J^x, J^y\}$, defined by

$$J^x = \frac{\partial}{\partial y}\left[\frac{\langle v_r^2\rangle - \langle u_r^2\rangle}{2}\right] + \frac{\partial}{\partial x}\langle u_r v_r\rangle, \tag{1}$$

$$J^y = \frac{\partial}{\partial x}\left[\frac{\langle v_r^2\rangle - \langle u_r^2\rangle}{2}\right] - \frac{\partial}{\partial y}\langle u_r v_r\rangle. \tag{2}$$

The vector provides a measure for the transport of vorticity. Figure 10 shows the effective vorticity flux density vectors $\tilde{J}^*$ at $x^* = 10$ and 20. $\tilde{J}^*$ is directed from higher to lower coherent vorticity concentration and its length indicates the strength of vorticity flux density. The vector and number above the left-hand upper corner in figure 10 provides correspondence between the vector length and magnitude.

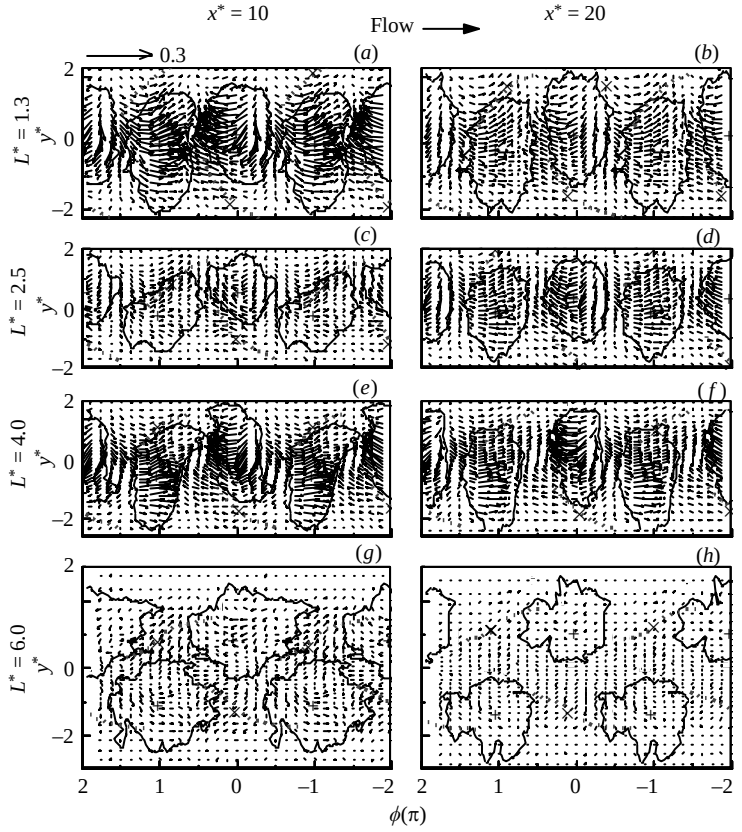

FIGURE 10. Effective vorticity flux density vectors $\tilde{J}^*$at $x^* = 10$ and 20. +, centres; saddles ×. The thicker solid line denotes the outermost vorticity contours in figure 7; the broken line indicates the diverging separatrix.

At $x^* = 10$, the maximum magnitude of the vector at $L^* = 1.3$ (figure 10*a*) exceeds twice that at $L^* = 4.0$ (figure 10*e*) and even more than at $L^* = 2.5$ (figure 10*c*) and 6.0 (figure 10*g*), internally consistent with the relatively large vorticity concentration at $x^* = 10$ for $L^* = 1.3$ (table 3 and figure 7). Furthermore, relatively long vectors associated with a vortex such as the one at $\phi = 0$, cross the vortex border and point towards the neighbouring vortex at $\phi = 1$ of opposite sign. On the other hand, long vectors associated with the vortex at $\phi = 1$ cross the vortex border and point at the vortex at $\phi = 0$. The observation indicates a vigorous exchange in vorticity or vorticity cancellation between adjoining opposite-signed vortices, which is probably responsible for the rapid vorticity decay at $L^* = 1.3$, dropping by 75 % from $x^* = 10$ to 20. At $L^* = 2.5$, relatively long vectors originating from the vortex at $\phi \approx 1$ tend to occur along the diverging separatrix through the saddle point, but do not interact strongly with those from the neighbouring vortex at $\phi \approx 0$, pointing to a weak vorticity exchange between oppositely signed vortices and hence a small vorticity cancellation. The maximum vector length at $L^* = 4.0$ is substantially longer than at $L^* = 2.5$. However, the vectors from opposite-signed vortices do not appear to be interacting vigorously, accounting for the slowly decaying vorticity concentration (figure 7*g–i*). At $L^* = 6.0$, relatively long vectors again occur along the diverging separatrix through the saddle point ($\phi \approx 1$), similarly to the $L^* = 2.5$ case. However,

because of a considerably larger vortex size, the vectors associated with the opposite-signed vortices interact with each other near the vortex border, implying a vorticity exchange and thus a faster vorticity decay than at $L^* = 2.5$ or 4.0.

At $x^* = 20$, the maximum vector length at $L^* = 1.3$ (figure 10*b*) reduces greatly compared with that at $x^* = 10$. Although the relatively long vectors still cross the border of the adjoining vortex, the vorticity concentration decays less rapidly than at $x^* = 10$ (figure 7*b*, *c*). In contrast, the vector length in the reattachment regime is longer at $x^* = 20$ (figure 10*d*, *f*) than at $x^* = 10$, in particular at $L^* = 2.5$. Accordingly, the vorticity decay is accelerated (figure 7*e–f*, *h–i*). At $L^* = 6.0$, the vectors (figure 10*h*) are very weak and show practically no interactions between oppositely signed vortices. In fact, the maximum coherent vorticity (figure 7*k*) approaches the background level and the vorticity decay is probably caused mainly by the viscous dissipation.

4.5. *Transport of momentum and heat*

4.5.1. *Coherent fluctuating velocities and temperature*

Figure 11 presents the phase-averaged velocity and temperature fluctuations $\tilde{u}^*$, $\tilde{v}^*$ and $\tilde{\theta}^*$ at $x^* = 10$. At $L^* = 1.3$, the $\tilde{u}^*$, $\tilde{v}^*$ and $\tilde{\theta}^*$ contours (figure 11*a–c*) resemble those previously reported behind an isolated cylinder (Matsumura & Antonia 1993; Zhou *et al.* 2002). The positive and negative $\tilde{u}^*$ contours display approximate up–down anti-symmetry about the vortex centre, while the $\tilde{v}^*$ contours are anti-symmetrical about $\phi = 0$. The positive $\tilde{\theta}^*$ concentration coincides well with the vortex, indicating a close association between the vortex and warm fluid. Note that the vortex is flanked downstream by the negative $\tilde{\theta}^*$ contours or cold fluid, resulting from the entrainment of cold fluid from the free stream by vortices.

At $L^* = 2.5$, the $\tilde{u}^*$, $\tilde{v}^*$ and $\tilde{\theta}^*$ contours (figure 11*d–f*) show patterns similar to those at $L^* = 1.3$. The detailed structures are, however, rather different. First, the $\tilde{u}^*$ contours display up–down anti-symmetry about the vortex centre at $\phi = 0$, but not so evident at $\phi \approx \pm 1$, probably because of the significantly weaker strength of vortices (figure 7*d*) than at $L^* = 1.3$ (figure 7*a*). Secondly, part of the positive isotherms overlaps with the vorticity concentration, while the other part, of relatively low level near the free stream, extends beyond the vortex border and points upstream, indicating the roll-up motion of warm shear layers separating from the heated upstream cylinder. In contrast, the positive isotherms at $L^* = 1.3$ are completely enclosed within the vortex, with the major axis of the contours approximately normal to the flow direction. As x^* increases to 20, the positive isotherms (not shown) coincide well with the vortex, similarly to the case of $L^* = 1.3$ (figure 11*c*). The observation points again to that at $L^* = 2.5$ the vortex formation is not completed until $x^* \approx 20$. Once again, the vortical structure is flanked downstream by the negative $\tilde{\theta}^*$ contours because of the arrival of cold fluid from the free stream. The $\tilde{u}^*$, $\tilde{v}^*$ and $\tilde{\theta}^*$ behaviours at $L^* = 4.0$ mimic those at $L^* = 2.5$ since both cases are in the reattachment regime. Nonetheless, unlike the case of $L^* = 2.5$, the $\tilde{u}^*$ contours exhibit up–down anti-symmetry about the vortex centre even at $\phi \approx \pm 1$, both $\tilde{u}^*$and $\tilde{v}^*$ contours are smooth, and the maximum $\tilde{\theta}^*$ coincides well with the vortex centre at $\phi \approx \pm 1$ as well as at $\phi = 0$, indicating a stronger vortex strength and quasi-periodicity, as evidenced in figure 4(*b*, *c*) and 7(*d*, *g*).

At $L^* = 6.0$, the $\tilde{u}^*$ contours (figure 11*j*) no longer show up–down anti-symmetry about the vortex centre, even at $\phi = 0$, and the $\tilde{v}^*$ contours (figure 11*k*) are least smooth, apparently caused by the weak vortex strength (figures 4*d* and 7*j*). The deviation between the maximum positive isotherms and the vortex centre is very

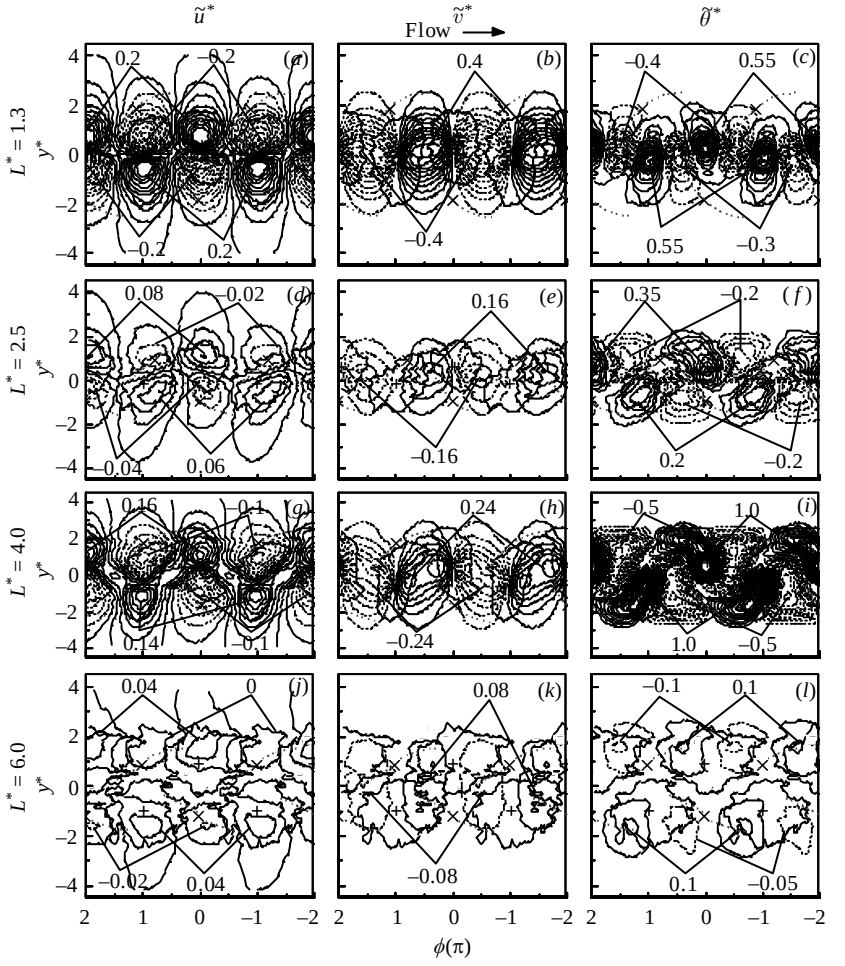

FIGURE 11. Phase-averaged velocity and temperature fluctuations at $x^* = 10$. (*a–c*) Contour interval = 0.02; 0.04; 0.05. (*d–f*) 0.02; 0.04; 0.05. (*g–i*) 0.02; 0.04; 0.05. (*j–l*) 0.02; 0.04; 0.05. The thicker solid line denotes the outermost vorticity contours in figure 7; the broken line indicates the diverging separatrix.

significant, that is, the warm fluid and the vortical structure tend to be dissociated since the vortex of weak strength is unable to retain heat.

4.5.2. *Coherent momentum and heat fluxes*

At $L^* = 1.3$, the contours of $\tilde{u}^*\tilde{v}^*$, $\tilde{u}^*\tilde{\theta}^*$ and $\tilde{v}^*\tilde{\theta}^*$ (figure 12*a–c*) display patterns, which are qualitatively the same as those at $L^* = 0$ reported by Matsumura & Antonia (1993). The clover-leaf pattern about the vortex centre of the $\tilde{u}^*\tilde{v}^*$ contours arises from the coherent velocity field associated with the vortical motion in a reference frame translating at U_c. On the other hand, the $\tilde{u}^*\tilde{\theta}^*$ contours are positive above the upper row vortex centre at $\phi = 0$ and, though rather weak, negative below, reflecting a connection between the positive $\tilde{u}$ and the warm fluid. The $\tilde{v}^*\tilde{\theta}^*$ contours appear anti-symmetrical about the vortex centre, owing to the association of both positive and negative $\tilde{v}$ (figure 11*b*) with the warm fluid. There is a small departure from the anti-symmetry. For instance, the negative concentration of $\tilde{v}^*\tilde{\theta}^*$ is weaker above

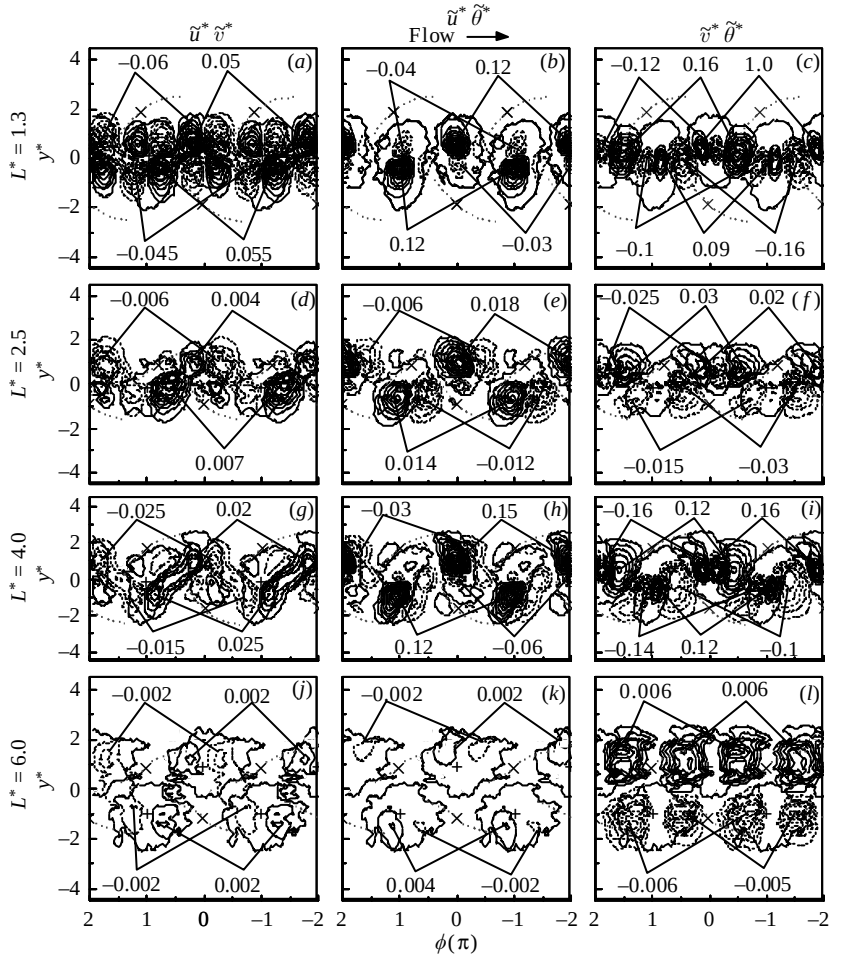

FIGURE 12. Phased-averaged coherent shear stress and heat fluxes ($x^* = 10$). (*a–c*) Contour interval = 0.005; 0.01; 0.02. (*d–f*) 0.001; 0.002; 0.005. (*g–i*) 0.005; 0.01; 0.034. (*j–l*) 0.001; 0.002; 0.001. The thicker solid line denotes the outermost vorticity contours in figure 7; the broken line indicates the diverging separatrix.

the centreline than the positive because the negative $\tilde{v}^*\tilde{\theta}^*$ region at $y^* > 0$ has more difficulty surviving where $\partial\Theta/\partial T < 0$. There is a strong concentration between two cross-stream vortices. For example, one positive concentration occurs between the upper-row vortex at $\phi = 0$ and the downstream lower-row vortex, resulting from the entrained cold fluid from the free stream ($\tilde{\theta} < 0$ and $\tilde{v} < 0$), which is evident in figures 11(*b*) and 11(*c*), respectively.

At $L^* = 2.5$, the $\tilde{u}^*\tilde{v}^*$ contours (figure 12*d*) associated with the vortex at $\phi = 0$ show a pattern similar to their counterpart at $L^* = 1.3$. However, the maximum magnitudes of $\tilde{u}^*\tilde{v}^*$, $\tilde{u}^*\tilde{\theta}^*$ and $\tilde{v}^*\tilde{\theta}^*$ are at least one order of magnitude smaller than at $L^* = 1.3$. The positive and negative contours are also less anti-symmetrical about the vortex centre. The increased departure from anti-symmetry may not necessarily give rise to a greater net contribution to $\overline{u^*v^*}$ because of the small maximum $\tilde{u}^*\tilde{v}^*$. The contours associated with vortices at $\phi \approx \pm 1$ display two lobes, instead of a clover-leaf pattern, apparently owing to weak vortex strength. Weak vortex strength also contributes

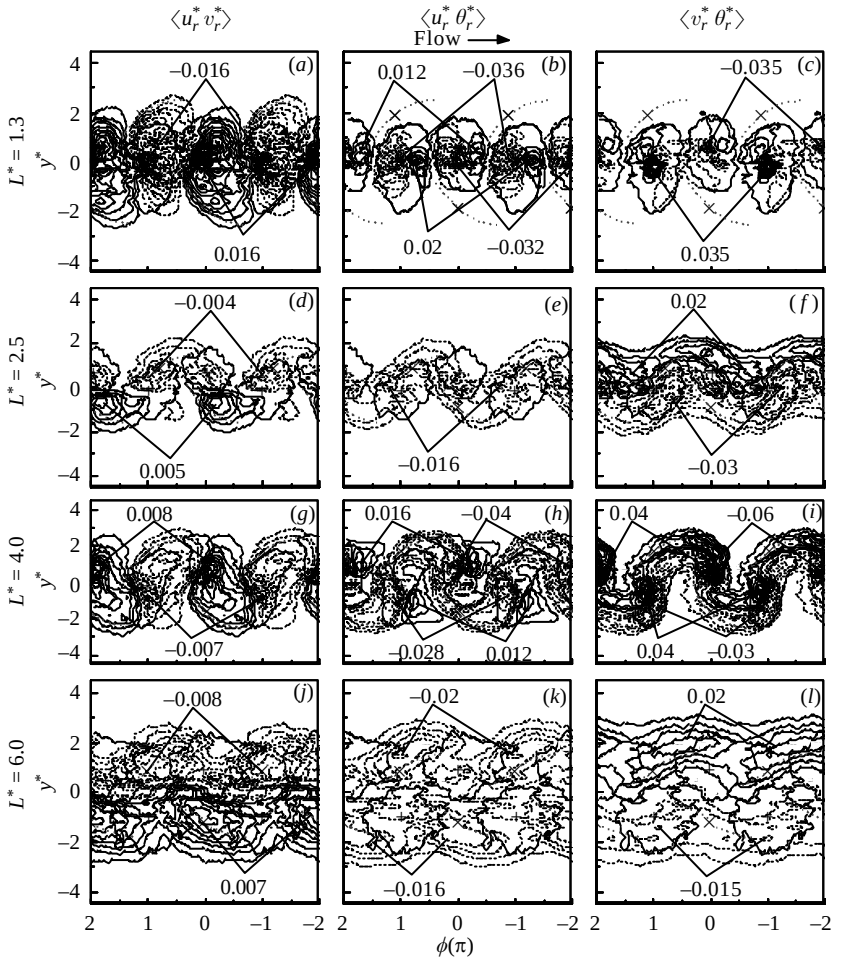

FIGURE 13. Phased-averaged incoherent shear stress and heat fluxes ($x^* = 10$). (a–c) Contour interval = 0.001; 0.004; 0.005. (d–f) 0.001; 0.004; 0.005. (g–i) 0.001; 0.004; 0.005. (j–l) 0.001; 0.004; 0.005. The thicker solid line denotes the outermost vorticity contours in figure 7; the broken line indicates the diverging separatrix.

to the absence of the positive $\tilde{v}^*\tilde{\theta}^*$ within the vortices at $\phi \approx \pm 1$ (figure 12f). At $L^* = 4.0$, however, the $\tilde{u}^*\tilde{v}^*$, $\tilde{u}^*\tilde{\theta}^*$ and $\tilde{v}^*\tilde{\theta}^*$ patterns (figures 12g–i) are largely similar to those at $L^* = 1.3$, with comparable maximum magnitudes. The $\tilde{u}^*\tilde{v}^*$ contours display a conspicuous departure from anti-symmetry about the vortex centre. This departure, coupled with the large maximum $\tilde{u}^*\tilde{v}^*$, implies a large contribution from vortices to $\overline{uv}$, as confirmed in § 5. The vortex strength at $L^* = 6.0$ is the weakest of all (see figure 7a, d, g, i). Consequently, the $\tilde{u}^*\tilde{v}^*$, $\tilde{u}^*\tilde{\theta}^*$ and $\tilde{v}^*\tilde{\theta}^*$ contours (figure 12j–l) appear very different from other cases, with the smallest maximum magnitude.

4.5.3. *Incoherent momentum and heat flux*

The $\langle u_r^* v_r^* \rangle$, $\langle u_r^* \theta_r^* \rangle$ and $\langle v_r^* \theta_r^* \rangle$ contours at $L^* = 1.3$ (figure 13a–c) again qualitatively resemble those at $L^* = 0$ (cf. figure 7a, d, g in Matsumura & Antonia 1993). For example, $\langle u_r^* v_r^* \rangle$ (figure 13a) tends to be concentrated around the vortex as well as the saddle point on the other side of the centreline. The $\langle u_r^* \theta_r^* \rangle$ contours (figure 13b)

exhibit the alternate occurrence of the positive and negative concentrations near the centreline, with the negative overwhelming, whereas the $\langle v_r^* \theta_r^* \rangle$ contours show concentrations around the vortex centre. The contours at $L^* = 2.5$ in figure 13(*d–f*) show some similarity to those at $L^* = 4.0$ in figure 13(*g–i*); their concentrations around the oppositely signed vortices are connected by contours aligned with the diverging separatrix (e.g. Hussain & Hayakawa 1987), showing a zigzag pattern, in conformity to the roll-up motion of shear layers. Yet, there is a discernible difference between the two cases. For instance, the $\langle u_r^* v_r^* \rangle$ pattern at $L^* = 4.0$ appears similar to that at $L^* = 1.3$, the opposite-signed contours occurring alternately in the streamwise direction. At $L^* = 2.5$, the $\langle u_r^* v_r^* \rangle$ concentrations, though occurring alternately in sign, do not appear to cross the centreline, with the negative and positive dominating above and below the centreline, respectively. The positive $\langle u_r^* \theta_r^* \rangle$ concentrations fail to show up. The $\langle u_r^* v_r^* \rangle$, $\langle u_r^* \theta_r^* \rangle$ and $\langle v_r^* \theta_r^* \rangle$ contours at $L^* = 6.0$ are distinct from the others, apparently because of the very weak vortex strength.

It is pertinent to point out that for all regimes there is a tendency for the negative $\langle u_r^* v_r^* \rangle$ to overwhelm the positive at $y^* > 0$, since the positive $\langle u_r^* v_r^* \rangle$ has difficulty surviving in a region where $\partial \overline{U}^* / \partial y^* > 0$; by the same token, the positive $\langle u_r^* v_r^* \rangle$ overwhelms the negative at $y^* < 0$, owing to $\partial \overline{U}^* / \partial y^* < 0$. For $\langle v_r^* \theta_r^* \rangle$, the positive contours generally dominate at $y^* > 0$, since the negative $\langle v_r^* \theta_r^* \rangle$ is suppressed in a region where $\partial \Theta^* / \partial y^* < 0$; at $y^* < 0$ where $\partial \Theta^* / \partial y^* > 0$, the negative dominates.

5. Reynolds stresses and heat fluxes

5.1. *Structural average*

The coherent contribution to the conventional or time-averaged Reynolds stresses, temperature variance and heat fluxes can be estimated based on the structural average. Assuming the phase-averaged structure beginning at the m_1 sample (corresponding to $\phi = -\pi$) before $\phi = 0$ and ending at the m_2 sample (corresponding to $\phi = \pi$) after $\phi = 0$, the structural average, denoted by a double overbar, is defined by

$$\overline{\overline{\tilde{q}\tilde{s}}} = \frac{1}{m_1 + m_2 + 1} \sum_{-m_1}^{m_2} \tilde{q}\tilde{s},$$

The value of $m_1 (= m_2)$ is 30 so that the duration $(m_1 + m_2 + 1)$ corresponds approximately to the vortex shedding period. The ratio of $\overline{\overline{\tilde{q}\tilde{s}}}$ to $\overline{qs}$ provides a measure for the transport characteristics of vortical structures.

5.2. *Fluctuating velocity and temperature variances*

Figure 14 presents the time-averaged, coherent and incoherent Reynolds stresses, temperature variance and heat fluxes at $x^* = 10$. The cross-stream distributions of $\overline{u^{*2}}$ (figure 14*a–d*), $\overline{v^{*2}}$ (figure 14*e–h*) and $\overline{\theta^{*2}}$ (figure 14*i–l*) are, in general, reasonably symmetrical about $y^* = 0$, similarly to the case of $L* = 0$. However, there is a significant difference in the maximum magnitude between the two- and single-cylinder wakes; the maximum $\overline{u^{*2}}$ (figure 14*a*) and $\overline{v^{*2}}$ (figure 14*e*) at $L^* = 1.3$ are about 0.038 and 0.16, respectively, considerably exceeding their counterparts, 0.027 and 0.07 (Zhou *et al.* 2002), respectively, at $L^* = 0$. While $\overline{v^{*2}}$ and $\overline{\theta^{*2}}$ show a single peak at $y^* = 0$, $\overline{u^{*2}}$ displays twin peaks (except at $L^* = 2.5$), mostly attributed to the two rows of vortices (figures 7 and 8), which is supported by the twin-peak distribution of $\overline{\overline{\tilde{u}^{*2}}}$ in all cases. As noted earlier in figure 7(*a, d, g, j*), the vortices at $L^* = 1.3$ and 4.0 are significantly stronger than two other cases, thus accounting for larger coherent contribution,

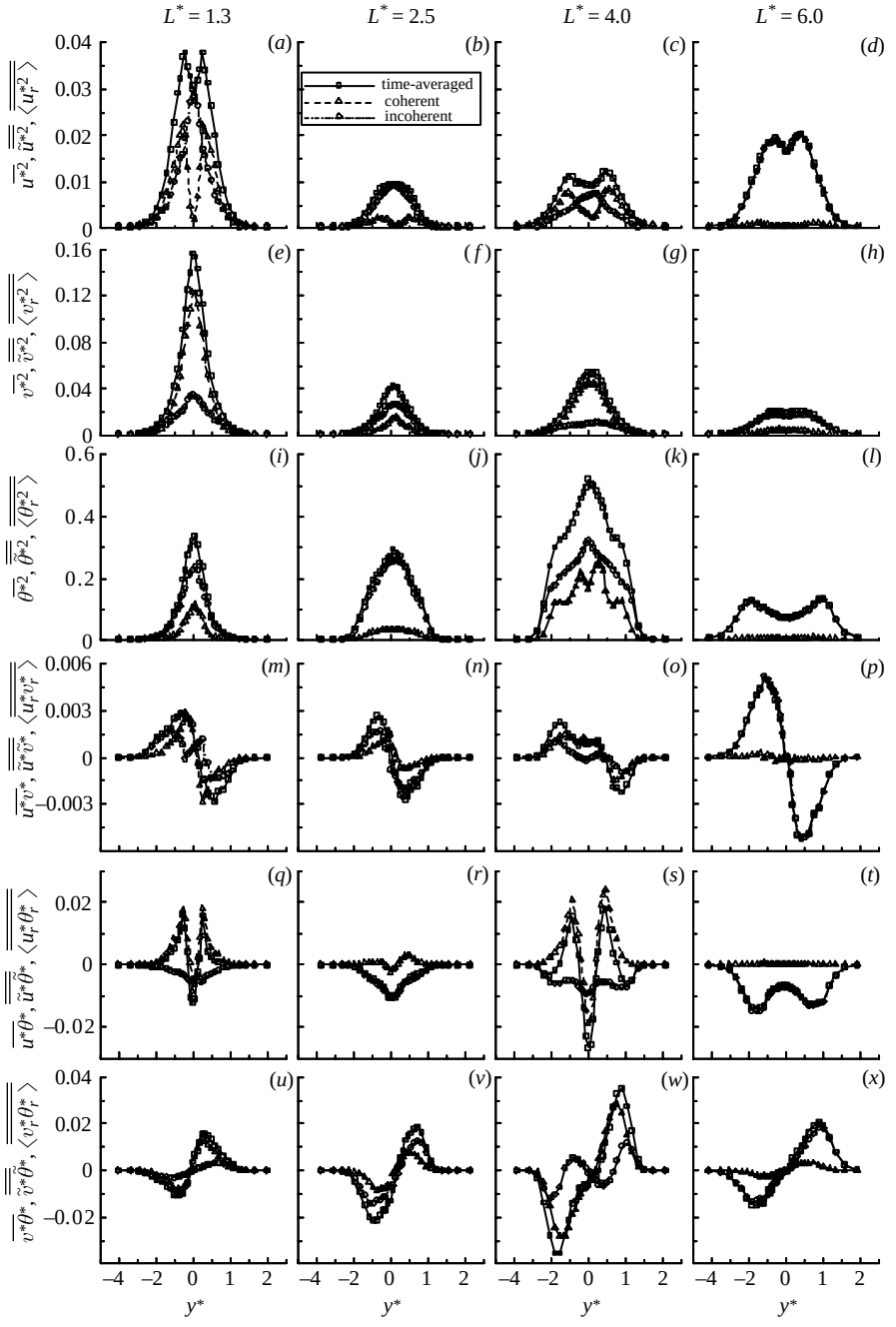

FIGURE 14. Time-averaged, coherent and incoherent Reynolds stresses, temperature variance and heat fluxes at $x^* = 10$.

i.e. $\overline{\overline{\tilde{u}^{*2}}}/\overline{u^{*2}}$, $\overline{\overline{\tilde{v}^{*2}}}/\overline{v^{*2}}$ and $\overline{\overline{\tilde{\theta}^{*2}}}/\overline{\theta^{*2}}$, than at $L^* = 2.5$ and 6.0. In all cases, $\overline{\overline{\tilde{v}^{*2}}}/\overline{v^{*2}}$ is greater than $\overline{\overline{\tilde{u}^{*2}}}/\overline{u^{*2}}$ or $\overline{\overline{\tilde{\theta}^{*2}}}/\overline{\theta^{*2}}$, like the case of a single-cylinder wake (Kiya & Matsumura 1985). There are two causes of this. First, $\tilde{v}$ overwhelms $\tilde{u}$ in the near wake owing to the primarily anti-symmetrical arrangement of the counter-rotating

vortices. Secondly, the vortical structures are presently detected based on the v-signal, and the coherent contributions to $\overline{u^2}$ and $\overline{\theta^2}$ are thus likely to be underestimated.

5.3. *Reynolds shear stress and heat fluxes*

The cross-flow distributions of $\overline{u^*v^*}$ (figure 14*m–p*) and $\overline{v^*\theta^*}$ (figure 14*u–x* are reasonably anti-symmetrical about $y^*=0$, whereas $\overline{u^*\theta^*}$ (figure 14*q–t*) is symmetrical about $y^*=0$. At $L^*=1.3$, the maximum $\overline{u^*v^*}$ (figure 14*m*), $\overline{u^*\theta^*}$ (figure 14*q*) and $\overline{v^*\theta^*}$ (figure 14*u*) are 0.003, 0.02 and 0.02, respectively, comparable to those at $L^*=0$ (Zhou *et al.* 2002). It is noteworthy that the coherent contribution at $L^*=1.3$ accounts almost entirely for $\overline{u^*v^*}$ for $y^*<0.5$ and remains significant for $y^*>0.5$; in contrast, this contribution at $L^*=0$ is very small. The result probably arises from longitudinally less anti-symmetrical $\tilde{u}^*\tilde{v}^*$ contours about the vortex centre at $L^*=1.3$ (figure 13*a*) than at $L^*=0$. The time-averaged heat fluxes may be ascribed largely to the coherent component, i.e. $\overline{\tilde{u}^*\tilde{\theta}^*}$ or $\overline{\tilde{v}^*\tilde{\theta}^*}$, which may be inferred from the contours of $\tilde{u}^*\tilde{\theta}^*$, $\langle u_r^*\theta_r^*\rangle$, $\tilde{v}^*\tilde{\theta}^*$ and $\langle v_r^*\theta_r^*\rangle$. The positive $\tilde{u}^*\tilde{\theta}^*$ (figure 12*b*) overwhelms the negative and its maximum is one order of magnitude larger than that of $\langle u_r^*\theta_r^*\rangle$ (figure 13*b*). The maximum $\tilde{v}^*\tilde{\theta}^*$ (figure 12*c*) also greatly exceeds that of $\langle v_r^*\theta_r^*\rangle$ (figure 13*c*). Owing to the cancellation of the positive and negative $\tilde{v}^*\tilde{\theta}^*$ contours within the vortex, the $\tilde{v}^*\tilde{\theta}^*$ concentration downstream of a vortex (figure 12*c*), which is positive above $y^*=0$ and negative below $y^*=0$, accounts for most of $\overline{\tilde{v}^*\tilde{\theta}^*}$. It may be concluded that, while transporting heat efficiently in both cases, the vortices transport momentum more effectively at $L^*=1.3$ than at $L^*=0$.

The maximum $\overline{u^*v^*}$ at $L^*=2.5$ is about the same as at $L^*=1.3$, though the maximum $\overline{u^*\theta^*}$ and $\overline{v^*\theta^*}$ are slightly larger. However, $\overline{\tilde{u}^*\tilde{v}^*}/\overline{u^*v^*}$, $\overline{\tilde{u}^*\tilde{\theta}^*}/\overline{u^*\theta^*}$ and $\overline{\tilde{v}^*\tilde{\theta}^*}/\overline{v^*\theta^*}$ at $L^*=2.5$ are considerably less than at $L^*=1.3$, which is expected because of the weak vortex strength at this L^*. At $L^*=4.0$, $\overline{u^*v^*}$, $\overline{u^*\theta^*}$ and $\overline{v^*\theta^*}$, along with their coherent contributions, show more similarity to the case of $L^*=1.3$ than to that of $L^*=2.5$, perhaps because of a vortex strength approaching that at $L^*=1.3$. Note that the maximum $\overline{u^*\theta^*}$ and $\overline{v^*\theta^*}$ are largest of all. Since the vortex strength at $L^*=6.0$ is weakest, their coherent contribution to $\overline{u^*v^*}$, $\overline{u^*\theta^*}$ and $\overline{v^*\theta^*}$ is essentially negligible.

It is worth pointing out that the contours of $\langle u_r^*\theta_r^*\rangle$ and $\langle v_r^*\theta_r^*\rangle$ at $L^*=4.0$ display a pattern in consistence with the shear-layer roll-up in the near wake. A similar pattern is evident at $L^*=2.5$, but absent at $L^*=1.3$ and 6.0. The observation corroborates our earlier proposition that, unlike the cases of $L^*=1.3$ and 6.0, the vortex formation is incomplete at $x^*=10$ for $L^*=1.3$ and 2.5.

5.4. *Streamwise evolution*

In view of the fact that $\overline{\tilde{q}\tilde{s}}/\overline{qs}$ depends on y^* as well as x^*, an averaged contribution at a fixed x^* from the coherent structure is defined, namely,

$$(\overline{\tilde{q}\tilde{s}}/\overline{qs})_m = \int_{-Y^*}^{Y^*} |\overline{\tilde{q}\tilde{s}}|\,\mathrm{d}y^* \Big/ \int_{-Y^*}^{Y^*} |\overline{qs}|\,\mathrm{d}y^*,$$

where $Y^*=5$ denotes the position where $|\overline{qs}|$ is considered to be zero. The calculated $(\overline{\tilde{q}\tilde{s}}/\overline{qs})_m$ for $x^*=10$, 20 and 30 is given in table 4. A number of observations can be made based on the data.

First, $(\overline{\tilde{q}\tilde{s}}/\overline{qs})_m$ is internally consistent with the observations from $\overline{qs}$, $\overline{\tilde{q}\tilde{s}}$ and $\langle\overline{q_r s_r}\rangle$ in figure 14. For instance, $(\overline{\tilde{v}^2}/\overline{v^2})_m$ is larger than $(\overline{\tilde{u}^2}/\overline{u^2})_m$ or $(\overline{\tilde{\theta}^2}/\overline{\theta^2})_m$. Secondly, $(\overline{\tilde{q}\tilde{s}}/\overline{qs})_m$ at $L^*=1.3$ is comparable at $x^*=10$ to that at $L^*=4.0$. However, $(\overline{\tilde{q}\tilde{s}}/\overline{qs})_m$

L^*	1.3			2.5			4.0			6.0		
x^*	10	20	30	10	20	30	10	20	30	10	20	30
$(\overline{\tilde{u}^2}/\overline{u^2})_m(\%)$	50	14	9	25	30	18	60	50	37	5	5	6
$(\overline{\tilde{v}^2}/\overline{v^2})_m(\%)$	71	31	19	27	48	29	74	72	64	13	5	1
$(\overline{\tilde{\theta}^2}/\overline{\theta^2})_m(\%)$	25	5	3	9	8	4	38	34	26	3	3	2
$(\overline{\tilde{u}\tilde{v}}/\overline{uv})_m(\%)$	60	21	6	34	45	23	71	68	66	4	2	1
$(\overline{\tilde{u}\tilde{\theta}}/\overline{u\theta})_m(\%)$	137	43	15	23	118	13	115	130	146	3	11	10
$(\overline{\tilde{v}\tilde{\theta}}/\overline{v\theta})_m(\%)$	74	31	15	33	38	23	83	78	64	14	5	1

TABLE 4. Averaged contributions from the coherent structure to Reynolds stresses, temperature variance and heat fluxes.

decays rapidly at $L^* = 1.3$, but very slowly at $L^* = 4.0$. For example, $(\overline{\tilde{v}^2}/\overline{v^2})_m$ drops by 73 % from $x^* = 10$ to 30 at $L^* = 1.3$, but only 13 % at $L^* = 4.0$. The quantity $(\overline{\tilde{u}\tilde{\theta}}/\overline{u\theta})_m$ at $L^* = 4.0$ grows all the way through up to $x^* = 30$. The disparity is not unexpected in view of their distinct vortex decay rates (figure 7*a–c*, *g–i*). Thirdly, $(\overline{\tilde{q}\tilde{s}}/\overline{qs})_m$ at $L^* = 2.5$ is well below that at $L^* = 4.0$ for all stations; for instance, its $(\overline{\tilde{v}\tilde{\theta}}/\overline{v\theta})_m$ is not more than half of that at $L^* = 4.0$. Furthermore, $(\overline{\tilde{q}\tilde{s}}/\overline{qs})_m$ increases considerably from $x^* = 10$ to 20 at $L^* = 2.5$, but varies little at $L^* = 4.0$. The different behaviours of $(\overline{\tilde{q}\tilde{s}}/\overline{qs})_m$ point to a difference in the initial conditions of the vortex formation between $L^* = 2.5$ and 4.0. Note that as a result of the slow decay, $(\overline{\tilde{q}\tilde{s}}/\overline{qs})_m$ at either $L^* = 2.5$ or 4.0 becomes larger at $x^* = 30$ than at $L^* = 1.3$. It is noteworthy that $(\overline{\tilde{u}\tilde{v}}/\overline{uv})_m$ at $L^* = 2.5$ or 4.0 as well as at $L^* = 1.3$ is comparable in magnitude to $(\overline{\tilde{v}\tilde{\theta}}/\overline{v\theta})_m$, in contrast with the $L^* = 0$ case where $(\overline{\tilde{u}\tilde{v}}/\overline{uv})_m$ is substantially smaller than $(\overline{\tilde{v}\tilde{\theta}}/\overline{v\theta})_m$ (Zhou *et al.* 2002). This implies that the vortices in a two-tandem-cylinder wake can transport momentum as effectively as heat. The implication is supported by the estimate of the turbulent Prandtl number $Pr_t \equiv (\overline{uv}/\partial\overline{U}/\partial y)/(\overline{v\theta}/\partial\overline{\Theta}/\partial y)$, which is 2.2, 1.0, 1.1 and 0.5 at $x^* = 10$ for $L^* = 1.3$, 2.5, 4.0 and 6.0, respectively. The corresponding $|\tilde{\omega}^*_{max}|$ is 1.18, 0.37, 0.83 and 0.24, respectively. The turbulent Prandtl number seems correlated to the vortex strength, the larger vortex strength corresponding to a higher Prandtl number. The vortex strength at $L^* = 6.0$ is comparable with that at $x^* = 40$ in a single-cylinder wake (Antonia, Zhou & Matsumura 1993). The corresponding Prandtl numbers are almost the same. The observation is reasonable since the vortex tends to retain heat, implying small heat transport (that is, the strong vortex is more likely to lead to a higher Prandtl number); heat transport out of the vortex is largely owing to the incoherent motion. Finally, $(\overline{\tilde{q}\tilde{s}}/\overline{qs})_m$ at $L^* = 6.0$ is very small, not exceeding 15 %, even at $x^* = 10$ and becomes essentially negligible for $x^* \geqslant 20$ owing to almost vanished vortical structures (figure 7*k*, *l*). In the co-shedding regime, the turbulent wake, including vortices, generated by the upstream cylinder impinges upon the downstream cylinder. As a result, the boundary layer around the downstream cylinder is probably turbulent, which may postpone the flow separation from the cylinder and subsequently result in relatively weak vortices. Therefore, the coherent contribution to $\overline{qs}$ is small. The observations essentially echo the streamwise evolution of vorticity contours (figure 7), reconfirm quantitatively the distinct evolution of the coherent structures and illustrate an important difference between the cases.

6. Different initial conditions and their effects on heat transport

6.1. *Difference in reattachment between* $L^* = 2.5$ *and* 4.0

It is the very different behaviours of the shear layers separating from the upstream cylinder that divide a two-tandem-cylinder wake into three distinct regimes. The results in figures 7–15 and table 4 demonstrate a marked difference between the flow structures at $L^* = 2.5$ and 4.0, each representing one of the two categories of the reattachment regime. The observation, along with the distinct *St–Re* relationships in the two flow categories reported by Xu & Zhou (2004) point to an important difference in the initial conditions of the vortex formation between the categories. In order to clarify this difference, the laser-induced fluorescence (LIF) flow visualization was conducted at $Re = 7000$ for $L^* = 2.5$ and 4.0, respectively, to capture the shear-layer reattachment on the downstream cylinder. A pin-hole of 0.5 mm diameter was drilled at about 45° from the leading stagnation point at the mid-span of the upstream cylinder tube. Smoke, generated from paraffin oil, of a particle size of about 1 μm in diameter was released from the pin-hole, thus providing seeding for flow above the centreline. Assuming approximate symmetry of shear layers about the centerline, no attempt was made to seed the flow on the other side of the centreline. A Dantec standard PIV2100 system was used to capture the flow images. More details of the LIF measurements were given in Cheng, Zhou & Zhang (2003). About 500 images were obtained for each L^*.

Figure 15 shows that reattachment of the shear layer from the upstream cylinder causes disturbance to the boundary layer around the downstream cylinder, which appears turbulent. An analysis of the images shows a difference in reattachment between the two cases. The shear layer separating from the upstream cylinder is more likely to reattach on the downstream side of the downstream cylinder at $L^* = 2.5$ (figure 15*a*), but on the upstream side at $L^* = 4.0$ (figure 15*b*). The different initial conditions are also reflected in the resultant drag coefficient of the two cylinders, estimated based on the cross-flow distributions of $\overline{U}$, $\overline{u^2}$ and $\overline{v^2}$ (Antonia & Rajagopalan 1990) at $x^* = 10$, which is 0.50 at $L^* = 2.5$ and 0.80 at $L^* = 4.0$ (0.83 at $L^* = 1.3$ and 1.34 at $L^* = 6.0$). Note that the fluid between the cylinders in this regime is relatively stagnant. At small L^* (say 2 to 3), the reattachment on the downstream side of the cylinder implies little room for the boundary layer to grow. Consequently, vortices formed behind the downstream cylinder are so weak that they continue to grow downstream under the effect of mean shear, as observed in figure 7(*d*, *e*). At large L^* (say 3 to 5), the reattachment on the upstream side of the cylinder allows the boundary layer around the cylinder to develop before separation. Naturally, the vortices (e.g. figure 7*g*) formed behind the downstream cylinder are stronger than at small L^* (e.g. figure 7*d*). Nevertheless, these vortices are still considerably weaker than at $L^* = 0$ (cf. figure 4*a* in Zhou *et al.* 2002) and thus continue to gain strength downstream under the effect of mean shear, but their relatively large initial strength should allow them to reach the maximum strength at a smaller x^* than at $L^* = 2.5$. The difference in the shear-layer reattachment location could also have an effect on the flow-separation location from the downstream cylinder, which subsequently affects the Strouhal number, the vortex strength and drag coefficient. It should be cautioned that more experimental or numerical data are needed to verify the above discussion.

6.2. *Heat transport*

The characteristics of heat transport can be examined by means of the coherent heat flux vector $\tilde{\boldsymbol{q}}^* = (\tilde{u}^*\tilde{\theta}^*, \tilde{v}^*\tilde{\theta}^*)$ (figure 16*b*) and the incoherent heat flux vector

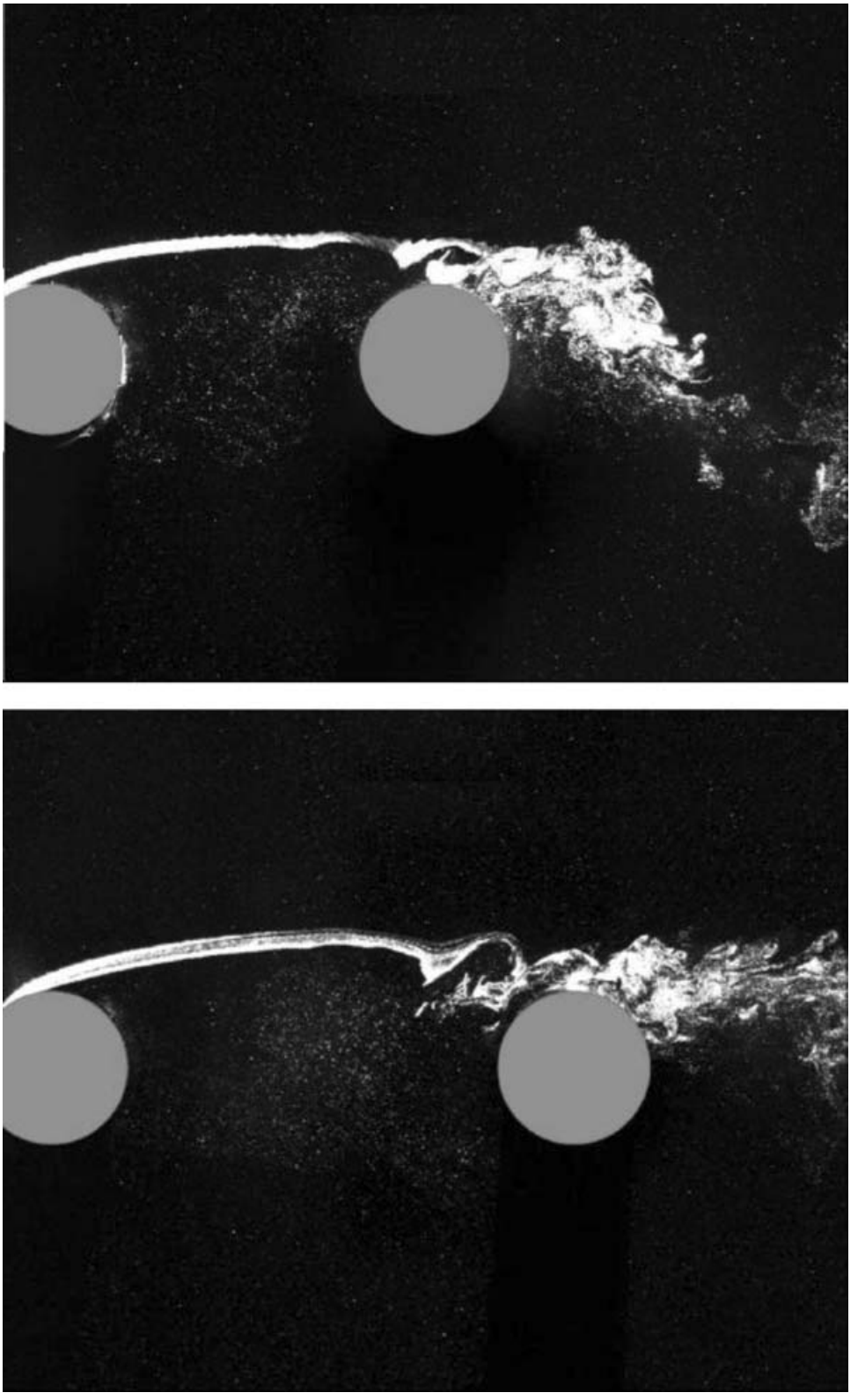

FIGURE 15. LIF flow visualization. (*a*) $L^* = 2.5$; (*b*) $L^* = 4.0$.

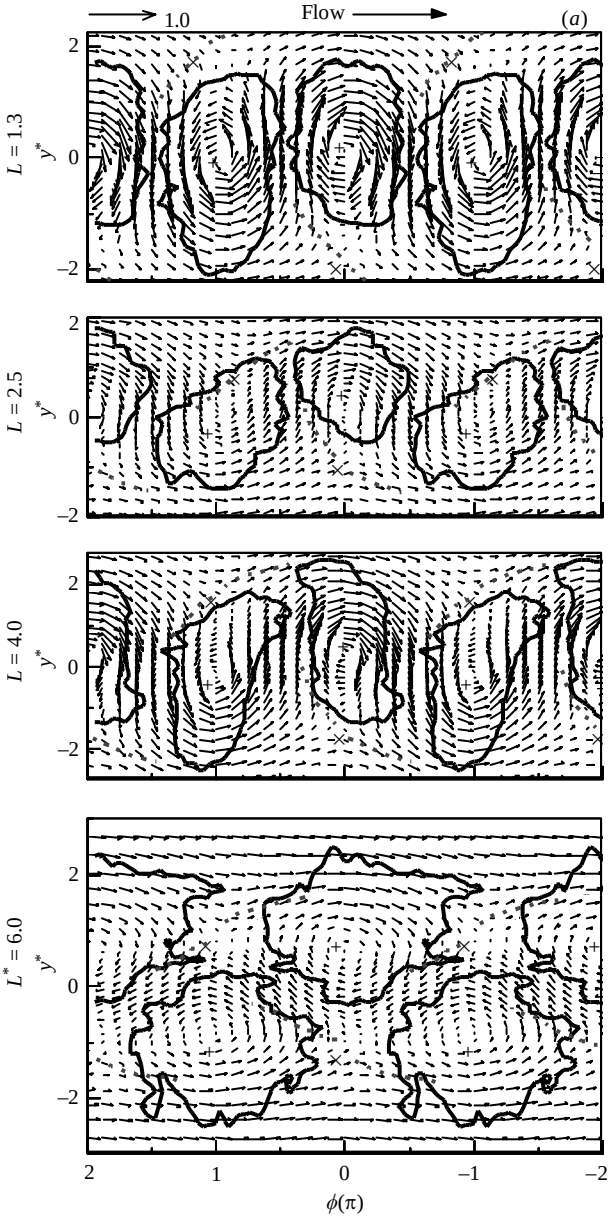

FIGURE 16(*a*). For caption see page 43.

$\tilde{\boldsymbol{q}}_r^* = (\langle u_r^* \theta_r^* \rangle, \langle v_r^* \theta_r^* \rangle)$ (figure 16*c*) along with the coherent velocity vector $\tilde{\boldsymbol{V}}^* = (\overline{U}^* + \tilde{u}^* - U_c^*, \tilde{v}^*)$ (figure 16*a*), where $\tilde{\boldsymbol{V}}^*$ is viewed in a reference frame translating at U_c. The arrow and number near the upper left-hand corner in figure 16 indicate the correspondence between the length and magnitude of the reference vector.

For all L^* values, $\tilde{\boldsymbol{q}}^*$ within vortices is largely aligned with $\tilde{\boldsymbol{V}}^*$, and barely discernible near the saddle points, suggesting that the coherent motion contributes little to net heat transport out of vortices. The behaviours of $\tilde{\boldsymbol{q}}^*$ at $L^* = 1.3$ and 4.0 are similar to each other, but appear distinct from those at $L^* = 2.5$ and 6.0. The difference is

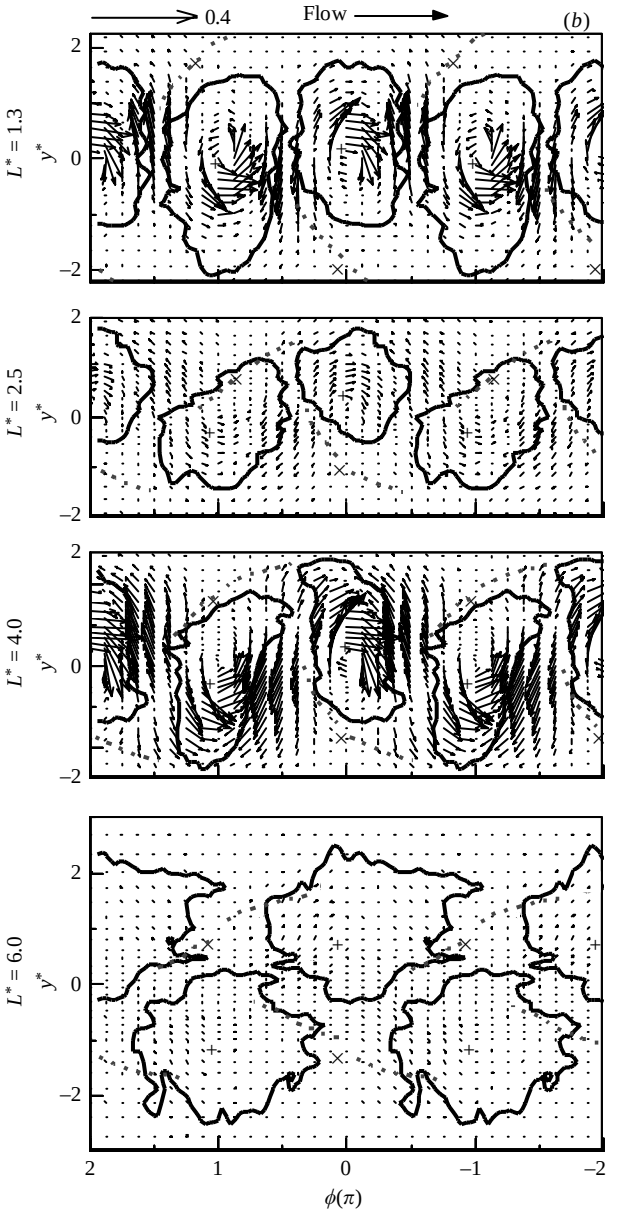

FIGURE 16(*b*). For caption see facing page.

apparently linked to the fact that the former are characterized by a vortex strength significantly higher than the latter. As evident in the vector plot, the maximum magnitude of $\tilde{\boldsymbol{q}}^*$ at $L^* = 1.3$ or 4.0 exceeds 3 times that at $L^* = 2.5$, and more when compared with the case of $L^* = 6.0$. The disparity is approximately commensurate with that between the vortex strengths (table 3) or that between the lengths of the effective vorticity flux density vectors (figure 10). Note that at $L^* = 1.3$ and 4.0, $\tilde{\boldsymbol{q}}^*$ in the alleyway between vortices is in a direction opposite to $\tilde{\boldsymbol{V}}^*$ and points towards the free stream, apparently arising from the entrainment of cold fluid from the free stream into the wake by vortices, as inferred from the $\Theta^* + \tilde{\theta}^*$ or $\tilde{\theta}^*$ contours in § 4.

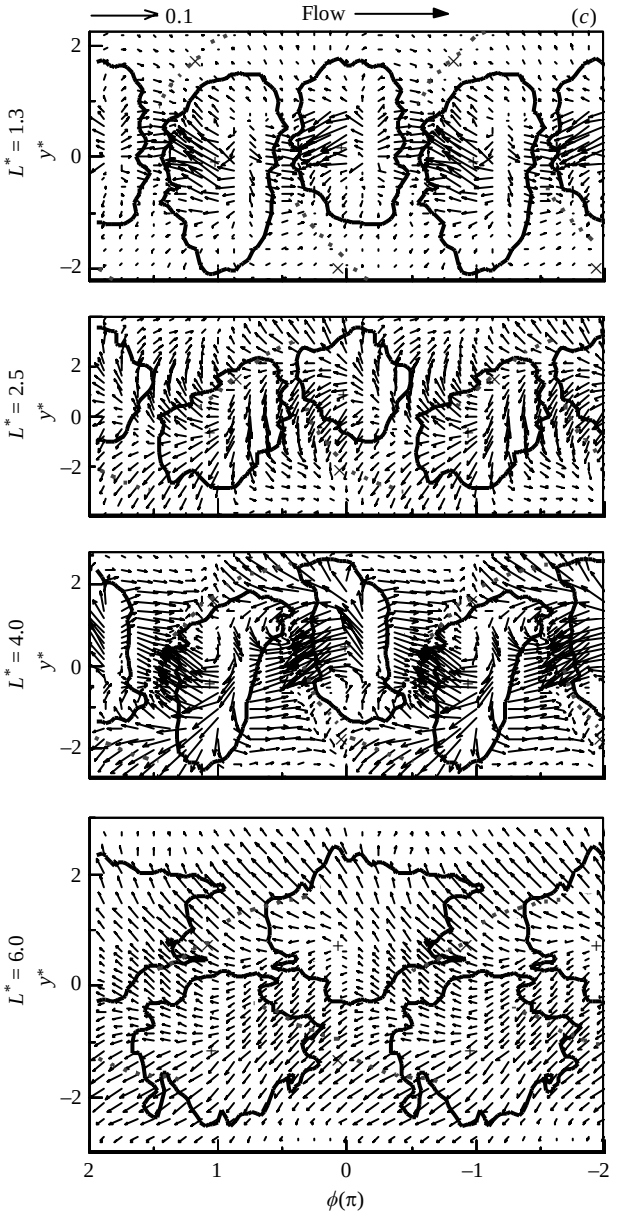

FIGURE 16. (*a*) Phase-averaged coherent velocity vectors $\tilde{\boldsymbol{V}}^*$ in a reference frame moving at U_c. (*b*) Phase-averaged coherent heat flux vectors $\tilde{\boldsymbol{q}}^*$. (*c*) Phase-averaged incoherent heat flux vectors $\tilde{\boldsymbol{q}}_r^*$ at $x^* = 10$. The broken line indicates the diverging separatrix.

The incoherent heat flux vectors, $\tilde{\boldsymbol{q}}_r^*$ (figure 16*c*), are totally different from $\tilde{\boldsymbol{q}}^*$. At $L^* = 1.3$, those relatively long within vortices generally point upstream across the vortex border; the corresponding $\langle u_r^* \theta_r^* \rangle$ component is negative, that is, $u_r > 0$ tends to correspond to $\theta_r < 0$, $u_r < 0$ corresponding to $\theta_r > 0$. Furthermore, the vectors of appreciable length along the flow direction cross the vortex border downstream, which is probably ascribed to the partial assimilation of the cold fluid, drawn from the free stream by the vortex, into the vortex, i.e. $\theta_r < 0$ and $u_r < 0$. It may be inferred from

the observation that the incoherent motion is mainly responsible for the net heat transport out of vortices, closely resembling that at $L^* = 0$ (Matsumura & Antonia 1993).

The vectors at $L^* = 4.0$ (figure 16*c*) behave differently. Other than those crossing the vortex border and pointing upstream (or downstream) as at $L^* = 1.3$, long vectors pointing upstream are seen crossing the vortex border towards the free stream. For example, at $\phi = 0 \sim 1$ above the centreline, the $\langle v_r^* \theta_r^* \rangle$ component of those upward-pointing vectors is positive, that is, $v_r > 0$ tends to correspond to $\theta_r > 0$ and $v_r < 0$ to $\theta_r < 0$. This means that the incoherent motion either acts to transport heat out of the vortex or brings cold fluid from the free stream into the vortex. The latter scenario is more likely in view of the shear-layer roll-up motion at this L^*, which is evident in the contours of $\langle v_r^* \theta_r^* \rangle$ (figure 13*i*). In comparison, this phenomenon is neither evident at $L^* = 1.3$ nor at $L^* = 0$, where the vortices have been completely formed at $x^* = 10$ and the shear-layer roll-up motion is unlikely to be vigorous.

The $\tilde{\boldsymbol{q}}_r^*$ pattern at $L^* = 2.5$ exhibits more similarity to that at $L^* = 4.0$ than at $L^* = 1.3$, which is not unexpected because of the same reattachment regime involved for $L^* = 4.0$ and 2.5. However, there is appreciable difference; the long vectors crossing the vortex boundary and pointing upstream at $L^* = 4.0$ (or 1.3) are not evident at $L^* = 2.5$. Furthermore, the vectors downstream of a vortex are directed towards the free stream at $L^* = 2.5$. The results suggest that the net heat loss out of vortices is predominantly attributed to $\langle u_r^* \theta_r^* \rangle$ at $L^* = 4.0$, but to $\langle v_r^* \theta_r^* \rangle$ at $L^* = 2.5$.

At $L^* = 6.0$, the vectors, $\tilde{\boldsymbol{q}}_r^*$, tend to point upstream and towards the free stream all over the place, showing little correlation with vortices, conforming to the very weak vortices in the co-shedding regime.

The vortex pattern and heat transport characteristics at $x/d = 10$ are summarized in figure 17 based on the plots of $\tilde{\boldsymbol{V}}^*$, $\tilde{\boldsymbol{q}}^*$ and $\tilde{\boldsymbol{q}}_r^*$ for the four flow categories. In all cases, the wake is characterized by a single vortex street. For convenience, the discussion is mainly focused on vortex A in figure 17. At $L^* = 1.3$ (figure 17*a*), cold fluid is drawn into the wake from free stream 1 under the combined coherent motions of vortices A and C via the alleyway downstream of vortex A. Part of the cold fluid is assimilated into the quadrants between I and IV owing to the incoherent motion. The coherent motion contributes little to the net heat transport out of the vortex. Most of heat is lost from quadrants II and III of vortex A owing to the incoherent motion. The overall picture is largely similar to a single-cylinder case (Matsumura & Antonia 1993).

Heat transport at $L^* = 4.0$ (figure 17*c*) mimics that at $L^* = 1.3$, except that there is considerable incoherent heat flux in quadrant II directed upstream and towards the free stream, which is linked to cold fluid entrainment into the vortex under the shear-layer roll-up motion.

Heat transport at $L^* = 2.5$ (figure 17*b*) is significantly different from that at $L^* = 1.3$ or 4.0. With a less coherent vortex, there is relatively weak engulfment of cold fluid from the free stream into the wake, resulting in the weak coherent heat flux in the alleyway downstream of vortex A. Again, the incoherent heat flux plays a dominant role in the net heat transport out of vortices. However, the incoherent heat flux out of quadrants II and III of vortex A appears to predominate because of the considerably less cold fluid assimilated into quadrants I and IV under the incoherent motion.

As L^* increases to 6.0, the coherent heat flux (figure 17*d*) is very weak and heat transport, owing to the incoherent heat flux, out of vortex A from quadrants I, II and III, displays similarity to the case at $L^* = 2.5$.

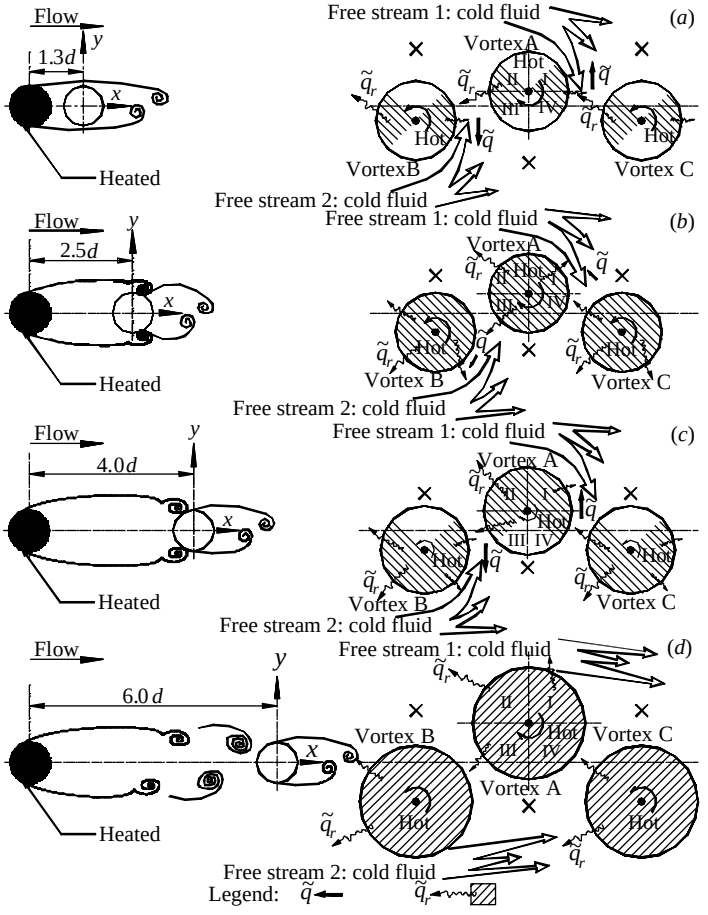

FIGURE 17. Summary sketch of the vortex pattern and transport. (*a*) 'Extended body' regime: $L^* = 1.3$; (*b*) shear layer reattachment on the after-body of the downstream cylinder: $L^* = 2.5$; (*c*) shear layer reattachment on the front-body of the downstream cylinder: $L^* = 4.0$; (*d*) co-shedding regime: $L^* = 6.0$.

7. Conclusions

The heat and momentum transport behind two tandem cylinders, with the upstream one slightly heated, have been measured using a three-wire probe in conjunction with a cross-wire for four different L^* ratios, i.e. 1.3, 2.5, 4.0 and 6.0, each representing one typical flow structure of this flow. The phase-averaged sectional streamlines and vorticity contours display one single vortex street, irrespective of the different flow regimes. However, there is a marked difference in the detailed flow structure, its downstream development, momentum and heat transport between the four cases, which is linked to distinct initial conditions in the vortex formation.

At $L^* = 1.3$, the free shear layers separated from the upstream cylinder overshoot the downstream cylinder and roll up to form a single vortex street. The effect of the downstream cylinder is likely to resemble that of a short splitter plate, which does not inhibit the vortex formation from the upstream cylinder. The vortex strength at $x^* = 10$ is about the same as its counterpart behind an isolated cylinder. However,

the presence of the downstream cylinder appears to accelerate the streamwise decay of vortices. The effective vorticity flux density vectors indicate vigorous interactions between adjacent oppositely signed vortices, resulting in a 75 % drop in the maximum vorticity $\tilde{\omega}^*_{max}$ from $x^* = 10$ to 20, appreciably higher than its counterpart (58 %) at $L^* = 0$.

In the reattachment regime, it is found that at $L^* = 2.5$ the shear layer from the upstream cylinder is more likely to reattach on the downstream side of the downstream cylinder, leaving little room for the boundary-layer growth. Subsequently, vortices after separation from the cylinder should initially be very weak. This is supported by the small vortex size and $\tilde{\omega}^*_{max}$ at $x^* = 10$, which is only 30 % of that at $L^* = 1.3$. The weak vortical structures correspond to weak interactions between vortices and hence a slow decay rate, which is confirmed by less vigorous interactions, compared with $L^* = 1.3$, between the effective vorticity flux density vectors of adjacent oppositely signed vortices. As a matter of fact, the vortical motion continues to grow, with its $\tilde{\omega}^*_{max}$ increasing from $x^* = 10$ to 20, probably under the roll-up effect of the shear layer in the wake. At $x^* = 30$, $\tilde{\omega}^*_{max}$ at $L^* = 2.5$ is almost the same as at $L^* = 1.3$.

As L^* is increased to 4.0, the shear layer is observed to reattach on the upstream side of the downstream cylinder. As such, there is room for the boundary layer to develop before separation from the cylinder. Naturally, the vortex strength at $L^* = 4.0$ is expected to be enhanced, compared with that at $L^* = 2.5$, but should not attain the level at $L^* = 1.3$; $\tilde{\omega}^*_{max}$ at $x^* = 10$ exceeds twice that at $L^* = 2.5$, but reaches only 70 % of that at $L^* = 1.3$. The vortex decay rate at$L^* = 4.0$ is as slow as at $L^* = 2.5$, giving rise to its $\tilde{\omega}^*_{max}$ at $x^* = 30$, doubling its counterpart at $L^* = 1.3$.

In the co-shedding regime, i.e. $L^* = 6.0$, vortices are characterized by a large size but small strength, its $\tilde{\omega}^*_{max}$ at $x^* = 10$ being only 20 % of that at $L^* = 1.3$. In this regime, the vortices generated by the upstream cylinder impinge upon and interact with those separated from the downstream cylinder. Such an interaction is likely to accelerate the decay of the vortex street, which virtually vanishes by $x^* = 30$.

The coherent contribution from vortices to the fluctuating velocity and temperature variances, the Reynolds shear stress and heat fluxes are examined. This contribution strongly depends on L^* or the flow structure and is to some extent commensurate with the vortex strength. At $L^* = 1.3$, the averaged coherent contribution at $x^* = 10$ is very significant, e.g. up to 50 %, 70 % and 25 % for $\overline{u^2}$, $\overline{v^2}$ and $\overline{\theta^2}$, respectively. The contribution drops rapidly with decaying vortex strength when x^* increases. This contribution at $L^* = 2.5$ is less significant than at $L^* = 1.3$, accounting for 25 %, 27 % and 9 % of $\overline{u^2}$, $\overline{v^2}$ and $\overline{\theta^2}$, respectively. However, the contribution to $\overline{u^2}$, $\overline{v^2}$ increases to 30 % and 48 %, respectively, from $x^* = 10$ to 20, internally consistent with the slightly increased vortex strength (figure 7*d*, *e*). As $L^*$is increased to 4.0, the coherent contribution is greatly enhanced, reaching 60 %, 74 % and 38 % at $x^* = 10$ to $\overline{u^2}$, $\overline{v^2}$ and $\overline{\theta^2}$, respectively, comparable with its counterpart at $L^* = 1.3$. Yet, unlike the case of $L^* = 1.3$, the contribution decays slowly downstream, as does the corresponding vortex strength. At $L^* = 6.0$, the contribution is negligibly small because of the very weak vortex strength. It has been reported in an isolated cylinder (Matsumura & Antonia 1993) that the vortices transport heat more efficiently than momentum. This difference diminishes at $L^* = 1.3$ where the averaged contribution to $\overline{uv}$ and $\overline{v\theta}$ is 60 % and 74 %, respectively, at $x^* = 10$, as versus 48 % and 84 % at $L^* = 0$ (Zhou *et al.* 2002). In the reattachment regime, however, the vortices appear transporting momentum almost as efficiently as heat. The averaged coherent contribution to $\overline{uv}$ and $\overline{v\theta}$ at $x^* = 10$ is 34 % and 33 % at $L^* = 2.5$ and 71 % and 83 % at $L^* = 2.5$, respectively. In this regime, the contours of $\tilde{u}\tilde{v}$ (figure 12*d*, *g*) are longitudinally less

antisymmetrical about the vortex centre, probably under the effect of the shear-layer roll-up motion, thus contributing more to $\overline{uv}$.

Y. Z. wishes to acknowledge support given to him by The Hong Kong Polytechnic University through grant G-YW74 and Research Grants Council of HKSAR through grant B-Q862. Dr G. Xu's contribution to experimental work is acknowledged.

REFERENCES

Antonia, R. A. Browne, L. W. B. Bisset, D. K. & Fulachier, L. 1987 A description of the organized motion in the turbulent far-wake of a cylinder at low Reynolds number. *J. Fluid Mech.* **184**, 423–444.

Antonia, R. A. & Orlandi, P. 2003 Effect of Schmidt number on passive scalar turbulence. *Appl. Mech. Rev.* **56**, 615–632.

Antonia, R. A. & Rajagopalan, S. 1990 A comment on the determination of drag of a circular cylinder. *AIAA J.* **28**, 1833–1835.

Antonia, R. A. Zhou, Y. & Matsumura, M. 1993 Spectral characteristics of momentum and heat transfer in the turbulent wake of a circular cylinder, *Exp. Thermal Fluid Sci.* **6**, 371–375.

Apelt, C. J. & West, G. S. 1973 The effects of wake splitter plates on the flow past a circular cylinder in the range $10^4 < R < 5 \times 10^4$. *J. Fluid Mech.* **61**, 187–198.

Apelt, C. J. & West, G. S. 1975 The effects of wake splitter plates on bluff-body flow in the range $10^4 < R < 5 \times 10^4$. Part 2. *J. Fluid Mech.* **71**, 145–160.

Arie, M., Kiya, M., Morya, M. & Mori, H. 1983 Pressure fluctuations on thesurface of two circular cylinders in tandem arrangement. Trans. *ASME J. Fluids Engng* **105**, 161–167.

Cheng, L., Zhou, Y. & Zhang, M. M. 2003 A perturbation on interactions between vortex shedding and free vibration. *J. Fluids Struct.* **17**, 887–901.

Ferré, J. A. & Giralt, F. 1989 Some topological features of the entrainment process in a heated turbulent wake. *J. Fluid Mech.* **198**, 65–78.

Grove, A. S., Shair, F. H., Petersen, E. E. & Acrivos, A. 1964 An experimental investigation of the steady separated flow past a circular cylinder. *J. Fluid Mech.* **19**, 60–80.

Hasan M. A. Z. & Budair, M. O. 1994 Role of splitter plates in modifying cylinder wake flows. *AIAA J.* **32**, 1992–1998.

Hussain, A. K. M. F. & Hayakawa, 1987 Eduction of large-scale organized structures in a turbulent plane wake. *J. Fluid Mech.* **180**, 193–229.

Igarashi, T. 1981 Characteristics of the flow around two cylinders arranged in tandem, 1st Report. *Bull. JSME*, B **24**, 323–331.

Kiya, M. & Matsumura, M. 1985 Turbulence structure in the intermediate wake of a circular cylinder. *Bull. JSME* **28**, 2617–2624.

Kolář, V., Lyn, D. A. & Rodi, W. 1997 Ensemble-averaged measurements in the turbulent near wake of two side-by-side square cylinders. *J. Fluid Mech.* **346**, 201–237.

Lewis, W. K. 1922 The evaporation of a liquid into a gas. *Trans. ASME* **14**, 445–446.

Mahir, N. & Rockwell, D. 1996 Vortex formation from a forced system of two cylinders. Part I: Tandem arrangement. *J. Fluid Struct.* **10**, 473–489.

Matsumura, M. & Antonia, A. 1993 Momentum and heat transport in the turbulent intermediate wake of a circular cylinder. *J. Fluid Mech.* **250**, 651–668.

Ohya, Y., Okajima, A. and Hayashi, M. 1989 Wake interference and vortex shedding. *Encyclopedia of Fluid Mechanics,* vol. 8, chap. 10, Gulph. pp 322–389.

Roshko, A. 1953 On the development of turbulent wakes from vortex streets. *NACA TN* 1191, pp. 1–25.

Roshko, A. 1955 On the wake and drag of bluff bodies. *J. Aero. Sci.* **22**, 124–132.

Roshko, A. 1961 Experiments on the flow past a circular cylinder at very high Reynolds number. *J. Fluid Mech.* **10**, 345–354.

Shraiman, B. I. & Siggia, E. D. 2000 Scalar turbulence. *Nature* **405**, 639–646.

Wang, Z. J., Zhou, Y., Wang, X. W. & Jin, W. 2003 A fibre-optic Bragg grating sensor for simultaneous static and dynamic temperature measurement on a heated cylinder in cross-flow. *Intl J. Heat Mass Transfer* **46**, 2983–2992.

Warhaft, Z. 2000 Passive scalars in turbulent flows. *Annu. Rev. Fluid Mech.* **32**, 203–240.

Xu, G. & Zhou, Y. 2004 Strouhal numbers in the wake of two inline cylinders. *Exps. Fluids* **37**, 248–256.

Yiu, M. W., Zhou, Y. & Zhu, Y. 2004 Passive scalar transport in a turbulent cylinder wake in the presence of a downstream cylinder. *Flow Turb. Combust.* **72**, 449–461.

Zdravkovich, M. M. 1977 Review of flow interference between two circular cylinders in various arrangements. *Trans ASME J. Fluids Engng* **99**, 618–633.

Zdravkovich, M. M. 1987 The effects of the interference between circular cylinders in cross flow. *J. Fluids Struct.* **1**, 239–261.

Zhou, T. Zhou, Y., Yiu, M. W. & Chua, L. P. 2003 Three-dimensional vorticity in a turbulent cylinder wake. *Exps Fluids* **35**, 459–471.

Zhou, Y. & Antonia, R. A. 1994 Critical points in a turbulent near-wake. *J. Fluid Mech.* **275**, 59–81.

Zhou, Y., Zhang, H. J. & Yiu, M. W. 2002 The turbulent wake of two side-by-side circular cylinders. *J. Fluid Mech.* **458**, 303–332.